Check for updates

Received: 15 April 2021 | Revised: 12 August 2021 | Accepted: 17 August 2021

DOI: 10.1002/jrs.6245

RESEARCH ARTICLE

Journal of RAMAN SPECTROSCOPY WILEY

# The perfection of Raman spectroscopic gas densimeters

**Ronald J. Bakker**

Resource Mineralogy, Department of Applied Geosciences and Geophysics, Montanuniversität Leoben, Leoben, Austria

**Correspondence**
Ronald J. Bakker, Resource Mineralogy, Department of Applied Geosciences and Geophysics, Montanuniversität Leoben, Peter-Tunner Str. 5, 8700 Leoben, Austria.
Email: bakker@unileoben.ac.at

**Abstract**

Raman spectroscopy can be used to determine density of gases, because the energy of fundamental vibrational modes is affected by intermolecular distances. The key problem is the estimation of exact peak positions of Raman bands, because the analyses require a precision that is mostly less than the pixel resolution of modern Raman spectrometers. A new method to determine peak positions of Raman bands and atomic emission lines in a discontinuous spectrum without numerical manipulations is tested in this study: modified scanning multichannel technique. Relocation of the gratings with a Sinus Arm Drive can be performed over a distance that is only a fraction of the pixel size that allows peak position estimations with precisions smaller than the pixel resolution and to determine the uncertainty in this estimation. This uncertainty was not determined in previous studies about gas densimeters, resulting in a large variety of inconsistent data. The new method is tested with fluid inclusions in quartz. A $CO_2$ density of 0.1477 ± 0.0006 g·cm$^{-3}$ and 0.8880 ± 0.0007 g·cm$^{-3}$ determined with microthermometry correspond to a Fermi dyad of 103.12 ± 0.27 cm$^{-1}$ and 104.71 ± 0.26 cm$^{-1}$. A $CH_4$ density of 0.3461 ± 0.0002 g·cm$^{-3}$ and 0.4011 ± 0.0001 g·cm$^{-3}$ correspond to peak positions of 2910.66 ± 0.12 cm$^{-1}$ and 2910.57 ± 0.12 cm$^{-1}$. The error in these numbers must be regarded as the best estimated uncertainties of peak positions, which are probably slightly adjusted to higher values due to mechanical irregularities of the Sinus Arm Drive in modern Raman systems.

**KEYWORDS**

$CH_4$, $CO_2$, gas densimeter, scanning multichannel technique

## 1 | INTRODUCTION

Raman spectroscopy of gases such as $CO_2$ and $CH_4$ can be used to determine their physical properties, such as described by the relationship between temperature, pressure, and density (e.g., previous studies[1,2,3,4] and reference therein). The energy of the vibrational modes of gas molecules[5] is dependent on intermolecular distances, as expressed in molar volume or density.[6,7] The density effect is directly related to temperature and pressure in unary fluid systems, as described in equations of state (e.g., Span and Wagner[8] and Setzmann and Wagner[9]). The key problem for the use of densimeters is the estimation of exact peak positions of Raman bands of gases and fluids. The obtained density of the gases from analysis of the wavenumber position of its Raman band is very

This is an open access article under the terms of the Creative Commons Attribution License, which permits use, distribution and reproduction in any medium, provided the original work is properly cited.
© 2021 The Author. *Journal of Raman Spectroscopy* published by John Wiley & Sons Ltd.

sensitive to minor shifts in the band position. The peak position variability is mostly less than the pixel resolution of Raman spectrometers, that is, less than the range of wavelengths detected by one pixel of a multichannel detector. For example, 1 $cm^{-1}$ variation in Raman spectra may correspond to a density modification of 0.43 $g{\cdot}cm^{-3}$ for $CO_2$ and 0.06 $g{\cdot}cm^{-3}$ for $CH_4$ (e.g., Sublett et al.[4]).

Peak positions can only be accurately determined if Raman band shapes are well-defined, and spectrometers are correctly calibrated. Several publications are considered key-studies for calibration of multichannel Raman spectrometers[10,11,12] and for spectral line shape reproductions.[13,14,15] Unfortunately, most publications about so-called gas densimeters do not take into account these key-studies or the concepts that they disclose, and mainly rely on curve-fitting techniques with probability distribution functions ("*PDF*") applied to Raman bands in discontinuous spectra that produce apparently high precisions and resolutions (e.g., Izraeli et al.[16]). The suggested approximately 10 times enhancement of the frequency resolution for peak position according to this technique is a misleading statement, that is even exaggerated by Fukura et al.[17] and Lin et al.[18] to an ambiguous factor 30 times of apparent improvement of precision. The application of this technique resulted in a wide variety of inconsistent mathematical relationships between fluid density of $CO_2$ and $CH_4$ and Raman peak position wavenumbers. Most publications do not provide sufficient information of spectrometer properties and calibration methods, and consequently, the published experimental data cannot be reproduced. The main objective of calibration is to assign one pixel of the CCD detector to a wavelength. Atomic emission lines are excellent features to perform these calibration procedures with well-defined wavelengths (e.g., neon[19]). The absence of peak position estimation methods for these atomic emission lines is a major shortcoming of previous studies. To overcome the inconsistency in gas densimeter equations, the mathematical equations presented in previous studies are proposed to be normalized to a standard value without a scientific justification (e.g., previous studies[1,2,20,21]). The standard value is suggested to consider a supposed systematic error of peak position estimations in individual Raman systems. Recently, Remigi et al.[22] suggested that the pixel resolution of the detector is the main factor that affects the correlation between peak position of Raman bands and gas density. However, the cause of this error and inconsistencies remains unexplored. A standard value can be obtained from fluid inclusions with known gas properties, as it can be determined by microthermometry, that is, the relationship between density and homogenization temperatures of liquid and vapor phases (e.g., Shepherd et al.[23]). The present study illustrates that the discrepancies, that is, the supposed systematic error, originate in insufficient knowledge about the uncertainty of individual measurements (cf. previous works[24,25]). The proper meaning of "uncertainty" in this study is further explained in supplementary material to distinguish it from statistical analyses (Section S1, Supporting Information). It will be demonstrated that the least-squares fitting method with *PDF's* is not a reliable mathematical procedure to estimate peak positions of neon emission lines, silicon, $CH_4$, and $CO_2$ Raman bands with an accuracy that is narrower than the spectral width detected by one pixel of the detector (pixel resolution) and that it does not give any information about the uncertainty of individual measurements. A new method is offered in the present study with the best possible reconstruction of line shapes (both emission lines and Raman bands) without shape changing filtering techniques, which are analyzed with multichannel detectors, and that also includes the possibility to determine the uncertainty in peak position measurements. In addition, the conventional state-of-the-art calibration methods of Raman systems are critically assessed and scrutinized with the considerations of the present study. It will be demonstrated that the supposed discrepancies between the mathematical formulations of gas densimeters are an artefact of numerical data processing, unknown uncertainties, and insufficient knowledge of the impact of a moveable gratings (instrument factor) on the detection method.

## 2 | DISCONTINUITY OF SPECTRA

Modern Raman spectrometers are equipped with optical multichannel detectors, such as charge-coupled devices (CCD). These CCDs are composed of two-dimensional arrays of pixels, which may collect an image of the slit of a Raman spectrometer (e.g., Turrell and Corset[26]). The spectral width of a pixel, that is, the limiting spectral resolution, for a given total wavelength range recorded in the image area of a detector is determined by the number of pixels parallel to the gratings dispersion (e.g., Tuschel[27]). Each pixel picks up a certain wavelength span defined by pixel size, gratings dispersion and focal length. Each pixel is assigned a specific wavelength that is positioned in its center. The resulting spectrum is discontinuous because the light energy is detected diode by diode (i.e., pixel by pixel) with specific surface areas (Figure 1). The disadvantages and advantages of multichannel detectors with respect to single-channel techniques were elucidated by, for example, Knoll et al.[13] Despite the numerous advantages of multichannel detectors, a continuous spectrum may define

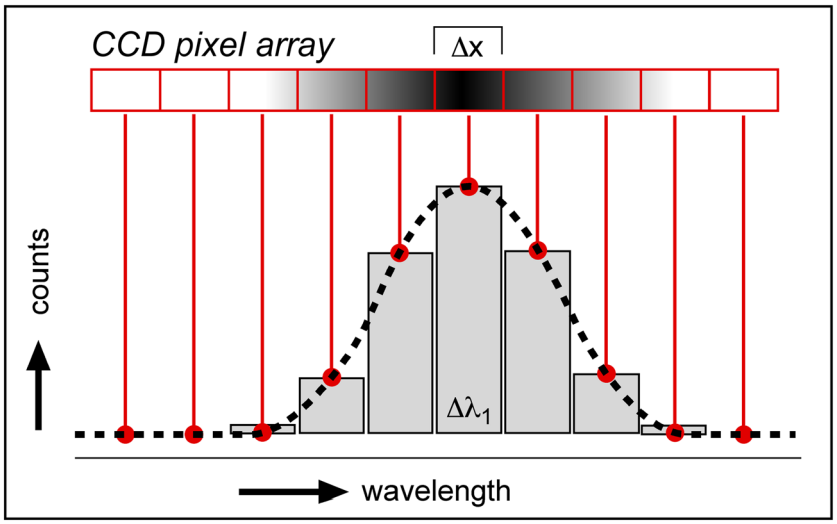


**FIGURE 1** Schematic image of the detection of a Raman band in a discontinuous spectrum. The shading in the CCD pixel array illustrates the intensity of specific wavelengths, each pixel has a size of Δx (e.g., 16 to 25 μm) and detects a wavelength range of $\Delta\lambda_1$, the vertical bars are the recorded intensities per pixel, and the dashed curve is a best-fit shape reproduction of these intensities [Colour figure can be viewed at wileyonlinelibrary.com]

more accurately shape properties, such as peak positions and intensities with a higher resolution. A nearly continuous spectrum of gases can be obtained by using single-channel detectors, controlled by precise adjustment of mechanical properties of the scanning technique in older types of Raman spectrometer systems.

The simplest interpretation of a discontinuous spectrum assigns a peak position to the pixel with the highest intensity (Figure 1). Consequently, the uncertainty in this position is defined by the pixel resolution. However, the intensity of neighboring pixels allows a refinement of peak position and its uncertainty (e.g., previous works[10,15]). For example, if a certain pixel has a distinct maximum, that is, neighboring pixel intensities are significant lower, this pixel number should be taken as the peak position. If two adjacent pixels have comparable intensities, the peak position can be assigned to a value at the center between these pixels.

The relationship between pixel number and wavelength is usually provided by the manufacturer of the spectrometer and can be adjusted according to integrated automatic and manual calibration procedures. These procedures may include as many standard lines as possible for which the wavelengths are accurately known, such as atomic emission lines (e.g., previous studies[28,29]). Statistical treatment of many peak values may result in a nearly linear pixel–wavelength relationship of the entire range in a spectral window,[10,30] with a calculated standard deviation of 0.2 pixel size. However, it must be noted that peak positions of individual neon lines are estimated according to the above mentioned "eye-determined" method,[11] with an individual uncertainty between one pixel and half a pixel. The estimated standard deviation (i.e., the use of statistics) is not illustrating the precision of individual measurements. Improvements in calibration methods have been the objective in several studies that mainly used peak shape analyses with least-squares fitting procedures.[11,29,30,31] Individual Raman bands were reproduced with polynomial functions (second- to fourth-order) fitted to the tip of a peak and with *PDF's* (e.g., Gaussian, Lorentzian) fitted to the entire band (e.g., Yuan and Mayanovic[32]). These best-fit reproductions provide peak position at maximum intensity, but do not consider uncertainty of each measurement.

## 3 | LASER WAVELENGTH UNCERTAINTIES

In Raman spectroscopy, three laser types are mainly used for the analyses of fluids and gases: (1) continuous wave gas laser (ion laser and $Ar^+$ laser); (2) gas laser (He–Ne laser); and (3) solid state laser (frequency doubled Nd–YAG laser). A well-defined wavelength of the laser is a prerequisite for accurate determination of Raman shifts (i.e., relative wavenumbers). Most studies only provide a synonym for the type of laser in terms of approximate wavelength, such as 514 nm for the $Ar^+$ laser,[4] 633 nm for the He–Ne laser,[33] and 532 nm for the frequency double Nd–YAG laser,[32,34] without specifying the exact wavelength. Other studies provide highly variable numbers on the accuracy in wavelength of the same type of lasers. For example, an $Ar^+$ laser was defined at 514.5 nm,[3,28,33,35] at 514.53 nm,[18,36,37] at 514.532 nm,[2,38,39,40] at 514.529 nm,[41] and at 514.5319 nm.[42] A He–Ne laser was defined at 632.9 nm[2] and at 632.8 nm,[39] and a Nd–YAG laser was defined at a constant value of 532.06 nm in all studies.[1,2,20,22,40,43,44]

It must be noted that gas lasers (He–Ne laser) and continuous wave ionized gas lasers ($Ar^+$ laser) emit

precisely known atomic emission lines, such as 514.5308 nm for Ar (NIST, Basic Atomic Spectroscopic Data) and 632.81646 ± 0.00004 nm[19] for Ne in the He–Ne laser. These lasers operate with an uncertainty of 0.001 nm. Solid-state lasers such as the Nd–YAG laser with a frequency doubled wavelength of about 532 nm cannot be produced with the same accuracy. The construction uncertainty of a 532.3-nm Nd–YAG laser is about ±0.3 nm (e.g., Oxxius, simply light, 2019; www.oxxius.com). The exact wavelength is affected by ambient conditions, such as temperature, pressure, and the refractive index of air.[45] It must be experimentally determined before any measurement session. This laser may shift its frequency substantially with time and temperature, and start-up modes of ±0.2 nm have been reported.[12] The uncertainty in wavelength is affected by stability of the laser, and certain types of laser regularly need calibration with reference lines. This concept is ignored in all previously mentioned studies with a Nd–YAG laser.

Insufficient specification of the laser wavelength is resulting in a systematic error of Raman band peak position estimation and calibration. A wavelength definition with a precision in the range of pm ($10^{-12}$ m) is needed to be able to obtain a wavenumber precision in $m^{-1}$, that is, an uncertainty in the range of a 0.01 $cm^{-1}$. A relatively small and significant change in peak position of gases with density, temperature, and pressure can only be detected if the laser wavelength is defined with an uncertainty in this range (pm).

The uncertainty in laser wavelength also affects the virtual relative wavenumber of neon lines, which are used for calibration. Moreover, reported wavenumbers are occasionally inconsistent with definitions of the laser wavelength. Virtual wavenumbers of neon lines are often indicated with a high accuracy that requires a laser definition with an exorbitant precision in the range of fm ($10^{-15}$ m). Zhang et al.[1] reported inconsistent wavelength and wavenumbers of neon lines: the 626.64952 nm neon line was erroneously defined as 626.56 nm that must yield a relative wavenumber of 2834.70 ± 0.25 $cm^{-1}$ according to the laser wavelength of 532.06 nm. However, a relative wavenumber of 2936.9888 $cm^{-1}$ was reported that correspond to an unrealistic highly overestimated precision of the laser wavelength at 532.060015 ± 0.000003 nm. Lamadrid et al.[2] and Sublett et al.[4] use the 543.3651 nm and 556.27662 nm neon line for additional compensation, which were assigned the relative wavenumbers 1031.42 $cm^{-1}$ and 1458.58 $cm^{-1}$ using a 514.532 nm $Ar^+$ laser. However, these wavenumbers correspond to a 514.529 nm laser and consequently result in a 0.12 $cm^{-1}$ systematic error.

## 4 | CALIBRATION METHODS BAZAR

Carter and Pemberton,[11] Carter et al.,[30] Zhang et al.,[1] and Liu et al.[46] already illustrated that not all aspects of calibration have been adequately addressed in literature. Unfortunately, there have been no significant improvements for gas densimeter calibrations during the last 30 years of research, as can be deduced from the overviews of Lamadrid et al.[2] and Zhang et al.[1] despite the development of improved machinery. Calibrations of individual Raman bands and entire wavelength range of spectrometers were performed with atomic emission lines, reference Raman bands, or a combination of both, but the variety of published calibration procedures is nearly equal to the number of publications.

Calibration methods that were performed separately from measurement sessions with gases, that is, the collection of reference spectra before, and after a session, were often used to document any modifications of the instrument setting in order to assign a specific wavelength (or wavenumber) to a specific pixel.[22,28,32,43,44,47,48] This calibration is often specified as a general "instrument calibration." These reference spectra were defined by neon lines that cover an entire spectral window (cf. Hutsebaut et al.[29]) or were defined by Raman bands (e.g., cyclohexane, naphthalene, benzonitrile, diamond, and silicon) and neon lines to calibrate only a small segment of that window. Multiple calibration methods were applied by Wang et al.[43] using separately measured benzonitrile peaks to correct the entire spectrum of $CO_2$ and using a simultaneously measured diamond peak to calibrate the main Raman band of $CO_2$. Yuan and Mayanovic[32] use an emission line of a fluorescent lamp (cf. standard room illumination) that was recorded separately from a fluid mixture. However, the wavelengths of fluorescence emission lines of these commercially available lamps are not as well defined as atomic emission lines and were calibrated themselves with a simultaneously recorded silicon Raman band. The separate detection of calibration lines and Raman bands of gases may introduce undefined irregularities due to variable laboratory conditions and spectrometer parameter properties.

Calibration methods that include a simultaneous measurement of both Raman bands and emission lines provide the most accurate estimations of wavenumbers and can be summarized by two procedures (Figure 2): calibration of the position (in $cm^{-1}$) of one specific Raman band (e.g., $\nu_1$ of $CH_4$) and calibration of a line segment, that is, the distance in $cm^{-1}$ between two Raman bands (e.g., the Fermi dyad of $CO_2$). The position of one specific Raman band was calibrated with:

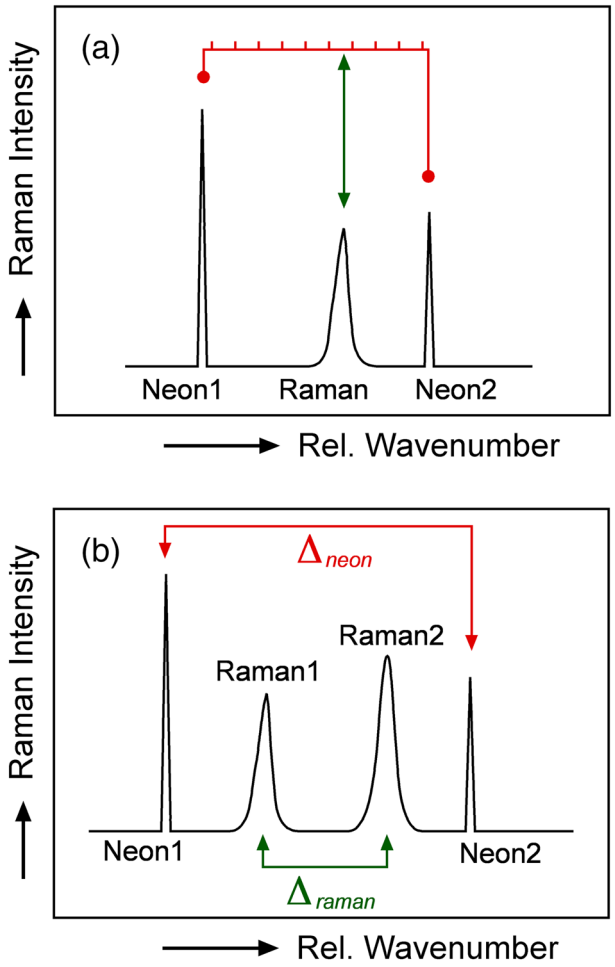


**FIGURE 2** Schematic representation of calibration methods; (a) proper bracketing technique of a Raman band between two neon lines (Equations 1 and 2); (b) line segment technique (Equation 3). See text for further details [Colour figure can be viewed at wileyonlinelibrary.com]

(1) distance (in $cm^{-1}$) to one atomic emission line,[20,37] (2) distance (in $cm^{-1}$) to one reference Raman band,[43] and (3) the bracketing technique using two emission lines on either site of the investigated Raman band.[3,4,18,41] A combination of 1 and 3 is used by Zhang et al.[1] and Itoh and Shirono[49] comparing the distance of a Raman band to one neon line with the distance between two neon lines, that is, a pseudo-bracketing technique. The calibration method of Lin et al.[18] is generally adopted in succeeding publications and assumes that the correction of the enclosed Raman band is the average of the deviation of two adjacent neon lines, and not proportional to the relative distance between the band and these lines. Consequently, any Raman band in between two neon lines is corrected with the same value. This method may result in significant erroneous corrections if the spectrum reveals a certain amount of nonlinearity within this range, and the Raman band is closer positioned to one of the neon lines. The "Lin" equation was also applied to the $CO_2$ spectrum by Fall et al.[41] and Sublett et al.,[4] but both $CO_2$ peak positions of the Fermi dyad are assigned equal correction values; consequently, the inferred Fermi dyad distance itself is not affected. Finally, some publications do not specify any calibration method, for example, $CO_2$ gas densimeters.[37,50]

An improved calibration with a proper bracketing technique is the definition of a linear equation that describes the correction factor as a function of wavelength or wavenumber in between two neon lines (Figure 2a). The general equation of this calibration method is

$$cor = a \cdot (\nu_{band})^{meas} + b \tag{1}$$

where *cor* is the difference between a measured value and a calibrated value (correction factor), $\nu$ is the relative wavenumber (in $cm^{-1}$), *band* represent the enclosed Raman signal of a specific gas, *meas* is measured value, $a$ and $b$ are constant values that can be determined with adjacent neon lines (Equation 2).

$$a = \frac{cor_{neon\,2} - cor_{neon\,1}}{(\nu_{neon\,2} - \nu_{neon\,1})^{meas}} \tag{2a}$$

$$b = \frac{(cor_{neon\,1} \cdot \nu_{neon\,2}) - (cor_{neon\,2} \cdot \nu_{neon\,1})}{\nu_{neon\,2} - \nu_{neon\,1}} \tag{2b}$$

where two neon lines (*1* and *2*) bracket the Raman band to be calibrated. A linear equation can be exactly defined with two neon lines (Equation 2). A simple linear regression can be applied using three to five adjacent neon lines to interpolate the correction of Raman bands at any position within the limits of this best-fit procedure. The correction factor (Equation 1) has to be added to the measured value to obtain a calibrated value.

The distance between two Raman bands, that is, a wavenumber line segment (Figure 2b), is calibrated with the distance between two neon lines positioned on either side of two investigated Raman bands[2,3] or both neon lines at higher wavenumbers.[40] The distance of the investigated bands is normalized to the reference distance between the neon lines. The general calibration equation is

$$(\Delta_R)^{cal} = (\Delta_R)^{meas} \cdot \frac{(\Delta_N)^{real}}{(\Delta_N)^{meas}} \tag{3a}$$

$$\Delta_R = \nu_{band\,2} - \nu_{band\,1} \tag{3b}$$

$$\Delta_N = \nu_{line\,2} - \nu_{line\,1} \quad (3c)$$

where $\Delta$ is the distance between two Raman bands ($R$) or neon lines ($N$), $\nu$ is the relative wavenumber (in $cm^{-1}$), *band* represent the Raman signals (*1* and *2*) of a specific gas, *line* represent neon emission lines (*1* and *2*), *meas* is measured value, *cal* is calibrated value, and *real* refers to reported value of emission lines.[19] This method is not able to calibrate peak positions of individual Raman bands.

The generally accepted method to estimate the peak position of Raman bands includes the use of best-fit procedures with symmetrical *PDF* to reproduce its shape. A common type of distribution curve is not presented in literature (e.g., Yuan and Mayanovic[32]). A Gaussian curve was used by Fukura et al.,[17] Wang et al.,[43] Shang et al.,[44] Lamadrid et al.,[2] and Hagiwara et al.[34]; a Lorentzian curve was used by Kawakami et al.[47] and Yamamoto and Kagi[48]; a combined Gaussian–Lorentzian curve was used by Lin et al.,[18] Fall et al.,[41] Wang et al.,[40] Le et al.,[37] and Sublett et al.[4]; a pseudo-Voigt curve was used by Remigi et al.[22] Some studies do not mention the method to reproduce shape properties and peak positions of Raman bands,[1,20,49,50] and none of the publications give information about the peak position estimation of atomic emission lines. The spectra of atomic emission "lines" are always defined by multiple pixels of the detector, comparable with a Raman band. The concept "line" is therefore misleading, and accurate peak positions must be analyzed with similar fitting procedures. In conclusion, the literature does not provide comparable calibration methods, which may have resulted in the apparent inconsistency of individual experimental data sets.

## 5 | METHOD LabRAM SYSTEM

Raman bands and atomic emission lines are analyzed with two types of Raman spectrometers in this study (Table 1): the LabRAM 300 (ISA Jobin Yvon, Horiba, 1998) and the LabRAM HR Evolution (Horiba Scientific, 2018). The number in brackets represents the year of acquisition of the spectrometer by the Montanuniversity Leoben (Austria). The main difference between these systems is the focal length: 300 mm for the LabRAM 300 and 800 mm for the LabRAM HR Evolution. Two types of laser are included in the Raman systems: He–Ne gas laser (632.816 ± 0.001 nm) and frequency doubled Nd–YAG solid state laser (532.0 ± 0.3 nm). The LabRAM 300 is equipped with an Andor detector (1024 × 255 pixels, pixel size 26 μm), and the latter system is equipped with two multichannel detectors: Synapse EM (1600 × 200 pixels, pixel size 16 μm) and Syncerity OE (1024 × 256 pixels, pixel size 26 μm). These multichannel detectors (CCD) are relatively small compared with the dispersion of diffracted light of the laser excitation source (Rayleigh scattering) and Raman bands (Stokes scattering). Consequently, the detector is only able to detect a relatively small range of wavelengths (i.e., a spectral window). Both systems are equipped with a movable grating system (Sinus Arm Drive, Horiba) to be able to measure different angles of diffraction, that is, different spectral windows at the same pixel position of the detector. Both systems use edge filters that absorb all light up to approximately 533.5 nm and 635 nm, corresponding to a cut-off at about 50 $cm^{-1}$ for both laser types. Both systems are equipped with a confocal hole, whereas a slit is not included in the LabRAM HR Evolution system. The LabRAM 300 and the LabRAM HR Evolution are operated with the software LabSpec 5 and LabSpec 6, respectively (Horiba, Jobin Yvon). Symmetric and asymmetric *PDF's* (Gaussian, Lorentzian, and combined

**TABLE 1** Specifications of the Horiba LabRAM Raman systems used in the present study

| Spectrometer | LabRAM 300 (1998) | LabRAM HR evolution (2018) |
|---|---|---|
| **focal length** | **300 mm** | **800 mm** |
| Gratings | 1800 lines/mm<br>600 lines/mm | 1800 lines/mm<br>600 lines/mm |
| Confocal hole | 1000 μm<br>500 μm | 100.021 μm<br>70.0087 μm<br>49.98 μm |
| Slit | 100 μm | - |
| Detector 1 | Andor DU 420-OE-322<br>Format: 1024 × 255 pixel<br>Pixel size: 26 × 26 μm | Synapse EM<br>Format: 1600 × 200 pixels<br>Pixel size: 16 × 16 μm |
| Detector 2 | - | Syncerity OE<br>Format: 1024 × 256 pixels<br>Pixel size: 26 × 26 μm |
| Laser 1 | Nd–YAG<br>532 nm[a]<br>(Laser Quantum, Ventus) | Nd–YAG<br>532 nm[a]<br>(Oxxius) |
| Laser 2 | - | He–Ne<br>632.816 nm (±0.001) |

[a]The exact wavelength of the Nd–YAG laser is estimated before each measurement session according to the method described in the text (paragraph 6.3).

Gaussian-Lorentzian) can be used to reproduce band shapes of raw spectra. The software PeakFit (v4.12, SYSTAT Software Inc.) is also used for this reproduction procedure, because it contains a larger variety of *PDF's*. The general equations that are used for fitting procedures in LabSpec 6 and PeakFit are given in the supporting information (Section S2). The source of specific atomic emission lines is an external neon lamp. Spectra are measured in 20 to 40 s with three accumulations in a single window, using Olympus microscope objectives MPlan N 100×/0.90 and LMPlanFI 100×/0.80. Both systems are initially calibrated with the position of the zero order of diffraction (0 nm) and a standard Raman band or an atomic emission line of neon (Section S3, Supporting Information). An important deficiency of this calibration procedure is that multiple rotation of the gratings over large angles cannot be controlled with a precision that is necessary to reproduce the exact position of specific reference Raman bands and emission lines (Section S4, Supporting Information). Peak position of the same neon line may shift up to 3 pm after rotation of the gratings back and forth (Table S1, Supporting Information).

It is preferred to use an atomic emission line for calibration, which has a better-defined wavelength (i.e., narrow band). The disadvantage of using Rayleigh scatter of the laser and of using the main Raman band of silicon is the unknown and relatively large uncertainty in their wavelength values (e.g., Nd–YAG laser, see preceding paragraph 3 "Laser wavelength uncertainties"). McCreery[39] illustrated that many reference Raman bands have standard deviations of approximately ±0.5 $cm^{-1}$ or higher for individual peak positions (ASTM values). This uncertainty does not allow a peak position calibration with a subpixel resolution. In the present study, laser, neon lines, and Raman bands are mainly evaluated in terms of wavelength (in nm) in the calibration procedure in order to omit any uncertainties in the excitation frequency of the laser.

## 6 | TESTING THE METHOD

The Raman spectrometers (Table 1) are tested with the generally accepted calibration method using best-fit Gaussian–Lorentzian curves for both Raman bands and atomic emission lines to obtain knowledge about the precision, accuracy, and uncertainty of individual peak position estimations. Synonyms for the wavelength of neon emission lines[19] are used in the following text: *529* = 529.81891 nm; *530* = 530.47580 nm; *532* = 532.63960 nm; *533* = 533.07775 nm; *534* = 534.10938 nm; *534a* = 534.32834 nm; *540* = 540.05616 nm; *565* = 565.66588 nm; *568* = 568.98163 nm; *571* = 571.922485 nm; *574* = 574.82985 nm; *576* = 576.44188 nm; *585* = 585.24878 nm; *626* = 626.64952 nm; *630* = 630.47893 nm; *633* = 633.44276 nm; *638* = 638.29914 nm; *640* = 640.22480 nm; *650* = 650.65277 nm; *653* = 653.28824 nm; *659* = 659.89528 nm; 667 = 667.82766 nm; *671* = 671.7043 nm; *692* = 692.94672 nm; *702* = 702.405 nm; *703* = 703.24128 nm.

### 6.1 | One point correction

The distance of a Raman band to one emission line close to that band can be used to calibrate the peak position.[20,32,37] For example, Figure 3 reveals the Raman band of silicon that is measured simultaneously with three neon lines. The *653* neon line is measured at 653.292 nm (deviation to theoretical value of +3.64 pm). This difference can be used as a constant correction value

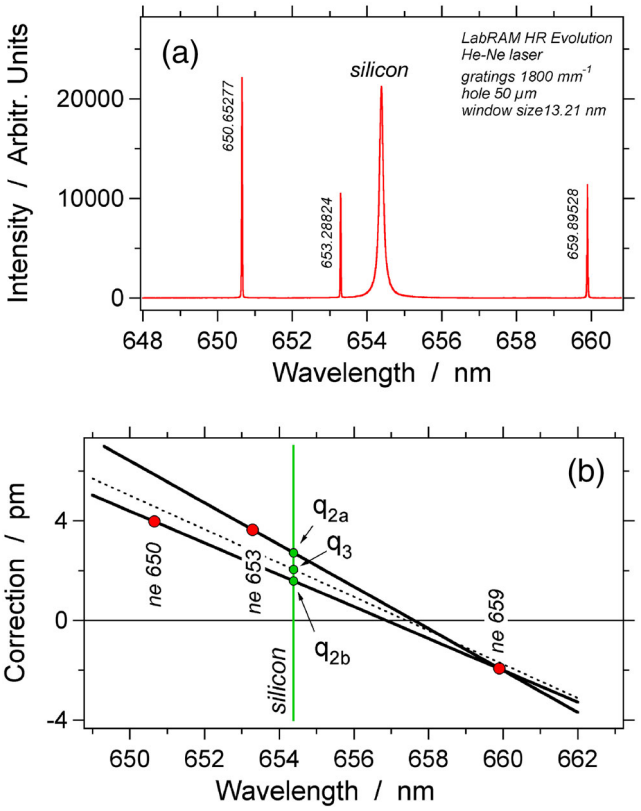


**FIGURE 3** (a) Raman spectrum of silicon with three neon emission lines (650.65277, 653.38824, and 659.89528 nm) that are used for the one-point correction and the bracketing technique. (b) Calibration of the silicon Raman band with the modified bracketing technique (Equations 1 and 2) using two reference neon lines, *653–659* and *650–659* (solid lines) or using a linear best fit through three neon lines: *650*, *653*, and *659* (dashed line). The correction values for the measured silicon wavelength are illustrated with $q_{2a}$, $q_{2b}$, and $q_3$ [Colour figure can be viewed at wileyonlinelibrary.com]

for the nearby silicon Raman band that is measured at 654.382 nm using the LabRAM HR Evolution system with a He–Ne laser and is subsequently calibrated to 654.378 nm (i.e., 520.70 $cm^{-1}$). Calibration with lines that are positioned at larger distances results in significant deviations in the corrected wavenumber of Raman bands, due to non-linearities of the spectrum. For example, a difference of −1.98 pm is estimated for the *659* neon line that results in a higher calibrated silicon wavenumber (520.83 $cm^{-1}$), whereas the *650* neon line has a difference of +3.98 pm that results in a lower calibrated silicon wavenumber (520.69 $cm^{-1}$). In general, one-point emission lines that are closer than 1 nm to the Raman band provide a comparable calibration accuracy of the proper bracketing method (Equations 1 and 2).

## 6.2 | Bracketing technique

The position of Raman bands can be calibrated by using two standard values on either side of the band measured within the same spectral window (cf. Figure 2a). A linear correction equation of the difference between measured and theoretical values of reference lines is estimated as a function of absolute wavelength (Equations 1 and 2). Subsequently, correction of enclosed Raman bands is calibrated by linear interpolation. This bracketing technique can be performed with several pairs of neon lines (Figure 3b). The linear best-fit through the *653* and *650* neon lines results in a correction of +2.72 pm at the wavelength of the silicon Raman band ($q_{2a}$ in Figure 3b). This correction corresponds to a relative wavenumber of 520.72 $cm^{-1}$. A difference of +1.59 pm is obtained by using the *650* and *659* neon lines ($q_{2b}$ in Figure 3b), resulting in a relative wavenumber of 520.75 $cm^{-1}$. This variability in calibrated peak positions of silicon Raman bands is smaller compared with the one-point correction with individual neon lines.

The bracketing technique can also be used to determine the wavelength of a reference neon line in between two other neon lines. This test is performed to illustrate the accuracy of this method by using well-defined neon lines[19] of both reference lines and the object to be determined by this method. The position of *653* neon line (653.28824 nm) is calibrated at 653.2893 nm according to the bracketing procedure with the *650* and *659* neon lines (Figure 3). Consequently, this method is able to reproduce wavelength of neon lines with an uncertainty of ± 1 pm, corresponding to ± 0.02 $cm^{-1}$ relative wavenumbers. The bracketing technique may be modified by including more than two reference lines by simple linear regression. For example, the three neon lines occurring in Figure 3a can be used to estimate a best-fit linear correction curve (dashed line in Figure 3b), which is slightly different from corrections based on only two reference lines. A correction of +2.05 pm is obtained for the silicon Raman band, compare the above-mentioned +1.59 and +2.72 pm. Multiple measurements of the silicon Raman band with this proper bracketing method result in an average wavelength of 654.380 ± 0.001 nm. It must be noted that the error in this number represents a reproducibility and not an uncertainty in individual measurements. The silicon Raman band itself (in nm) can be used as a reference value for the calibration of other Raman spectra by using a He–Ne laser with the excitation wavelength of 632.816 nm (±0.001). The corresponding relative wavenumber of silicon is 520.74 ± 0.05 $cm^{-1}$.

## 6.3 | Laser wavelength calibration

The He–Ne laser and the Nd–YAG lasers are calibrated with neon emission lines according to the one-point correction method (paragraph 6.1) and the bracketing method (paragraph 6.2) (Section S5, Supporting Information). An edge-filter blocks any signal in the anti-Stokes scattering range; therefore, the laser wavelength (i.e., Rayleigh scattering) can be estimated by using the one-point calibration with neon lines at higher wavelengths (Figures S8a and S9a, Supporting Information). The laser wavelength can also be estimated with the bracketing technique if the neon lamp is placed behind the edge filter (or notch filter) in the LabRAM system. Consequently, emission lines in the anti-Stokes region can also be detected, and the signal of the laser (Rayleigh scattering) can be bracketed (Figures S8b and S9b, Supporting Information). Multiple calibrations of the He–Ne laser using the bracketing technique result in wavelengths between 632.813 and 632.818 nm, with an average of 632.816 ± 0.003 nm. The calibrated wavelength of the Nd–YAG laser varies significantly between individual measurement sessions. For example, a calibrated wavelength of 532.059 ± 0.005 nm could not be reproduced the following day, that revealed wavelengths of 532.113 ± 0.006 nm. Each session has a laser wavelength reproducibility of about 6 pm, that is, approximately twice as much as the uncertainty of the He–Ne laser. The examples illustrate that the Nd–YAG laser has to be experimentally determined before any measurement session and that it is very unlikely that it has a constant wavelength over longer periods of investigation (cf. 532.06 nm[1,2,20,22,40,43,44]).

## 6.4 | Internal spectral window irregularities

The transition of wavelength to a pixel number in a fixed rotation angle of the gratings (i.e., an anchored spectral window position) is defined by linear dispersion of the gratings. However, the wavelength spacing of the dispersed light is slightly non-uniform in the entire range of detector pixels. For example, a pixel may detect a wavelength span of 0.047 nm in the left part and 0.045 nm in the right part of a window. Consequently, a variation of maximally 2 pm can be accounted for this effect. This may correspond to a wavenumber range variation in one pixel of 1.46 to 1.20 $cm^{-1}$ (e.g., Tuschel[27]). Dependent on the angle of dispersion and rotation of the gratings, the same wavelength interval will be detected by a slightly larger or smaller array of pixels. This nonlinearity does not affect the estimation of Raman band peak positions because each pixel is assigned a specific range of wavelengths.

Both Raman systems, that is, LabRAM 300 and LabRAM HR Evolution, reveal a significant shift in neon lines according to the relative position within a spectral window that largely exceeds this variability: a line positioned in the center occurs at significant different values compared with its position at the far-left or far-right side of a spectral window (see Section S6, Supporting Information). For example, Figure S10 (Supporting Information) illustrates the silicon Raman band and neon lines measured in two different spectral windows that are used to determine this variation. A variation of approximately 30 to 40 pm of neon emission lines is observed with both the LabRAM 300 system (Nd–YAG laser, 1800 $mm^{-1}$ gratings, Figure 4a) and the LabRAM HR evolution system (He–Ne laser, 600 $mm^{-1}$ gratings, Figure 4b) (Figure S11a, Supporting Information). The latter system also reveals a variation of approximately 10 pm with the Nd–YAG laser and 1800 $mm^{-1}$ gratings (Figure S11b, Supporting Information). The silicon Raman band and other neon lines reveal a similar shift, which reduces the variation of calibrated values to about 6 pm. The silicon band in Figure S10 (Supporting Information) is bracketed by the *540* and *556* neon lines and calibrated to wavelength values between 547.193 and 547.199 nm according to the range of spectral windows. The result is slightly improved (547.194 to 547.197 nm) if the intensity of neon lines is increased, in order to better characterize peak shape properties and distinguish them from background noise. It must be noted that the systematic variation is within the wavelength range detected by one pixel.

The question may arise if this variability is affecting the distance between neon lines and Raman bands (wavelength segments), which is a fundamental ingredient of calibration procedures. The distance between two neon lines that are closely positioned (i.e., less than 2 nm distance) reveal only minor modifications: a variability of approximately 2 pm (Figure 5a), whereas lines separated by about 10 nm reveal a variability up to 10 pm (Figure 5b). In terms of wavenumber, the distances may vary 0.05 $cm^{-1}$ and 0.23 $cm^{-1}$, respectively.

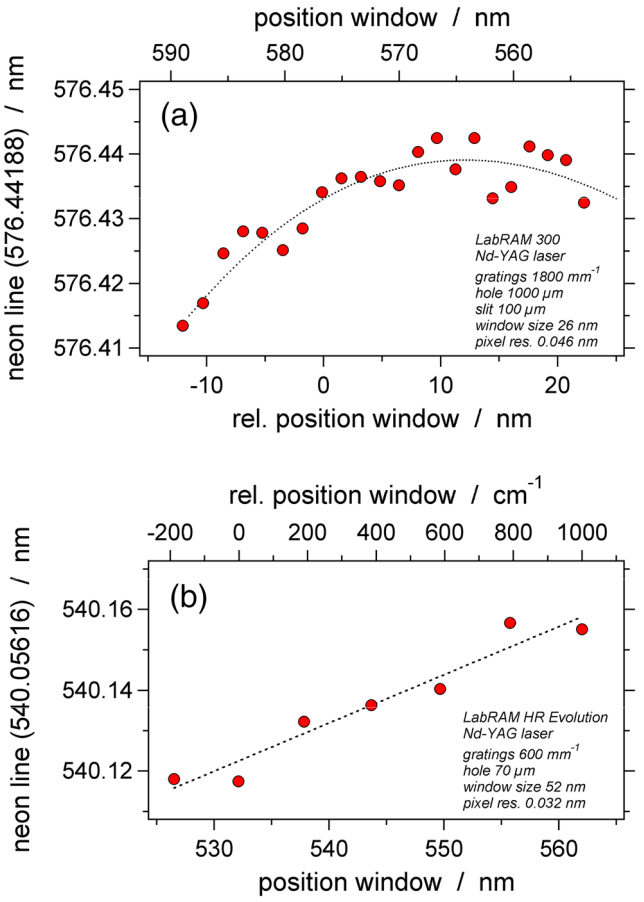


**FIGURE 4** Shift in the detected peak positions of neon emission lines 576.44188 nm (a) and 540.05616 nm (b) dependent on their position within a single spectral window. The position is specified in absolute wavelength and in a relative number. The latter is defined by the relative position of the neon line within a spectral window (in nm): 0 is the center position, positive values represent lines that appear to the right site, and negative values to the left site [Colour figure can be viewed at wileyonlinelibrary.com]

## 6.5 | Calibration with incorrect wavenumber of reference Raman bands

Silicon can be used to perform the principle automatic calibration procedure with the LabSpec software (see paragraph 5 "Method LabRAM system"). The relative wavenumber of the main peak of silicon is defined by

Dubessy et al.[33] at 520.7 ± 0.5 $cm^{-1}$ referring to Parker et al.[51] This first-order optical vibration of silicon was however defined at 520.2 ± 0.5 $cm^{-1}$ by Parker et al.[51] and is highly variable with temperature and crystallinity of the silicon.[52] A consequence of calibrating with an erroneous wavenumber is the incorrect positioning of neon lines in a Raman spectrum. For example, three sets of measurements session with a He–Ne laser are performed to estimate wavelengths of several neon lines (Figure 6), calibrated with silicon at 520.2 $cm^{-1}$, 520.7 $cm^{-1}$, and 521.2 $cm^{-1}$, according to the uncertainty given by Dubessy et al.[33] The position of neon lines is estimated at a central position within a spectral window. Each session results in significant different values of the "coeff" parameter defined by the general calibration procedure in LabSpec (cf. Section S3 in Supporting Information). The theoretical wavelength of the silicon Raman band is calculated at 654.3995 nm according to the 521.2 $cm^{-1}$ reference. As a consequence, wavelengths of neon lines occur systematically at higher values (+27 pm). A similar deviation with opposite sign is obtained through assigning the silicon wavelength a value of 654.3570 nm according to the 520.2 $cm^{-1}$ reference: Neon lines occur systematically at lower wavelengths (−22 pm). A nearly correct position of neon lines is obtained through calibration with silicon wavelength at 654.3782 nm according to the 520.7 $cm^{-1}$ reference, with an average deviation of +4 pm. In conclusion, peak positions of neon lines are estimated at incorrect wavelengths if the "coeff" parameter is determined with incorrect Raman band wavenumbers. The use of reference Raman bands with relatively large uncertainties, specified as standard deviation of an average value (e.g., McCreery[39]), result in uncertainties of approximately ±25 pm to ±50 pm in the wavelength estimation of neon lines, corresponding to approximately ±0.53 $cm^{-1}$ to ±1.51 $cm^{-1}$ wavenumber. Consequently, Raman band peak positions of gases such as $CO_2$ and $CH_4$ that are calibrated with these incorrect neon lines include a significant systematic error according to an incorrect definition of the reference Raman band.

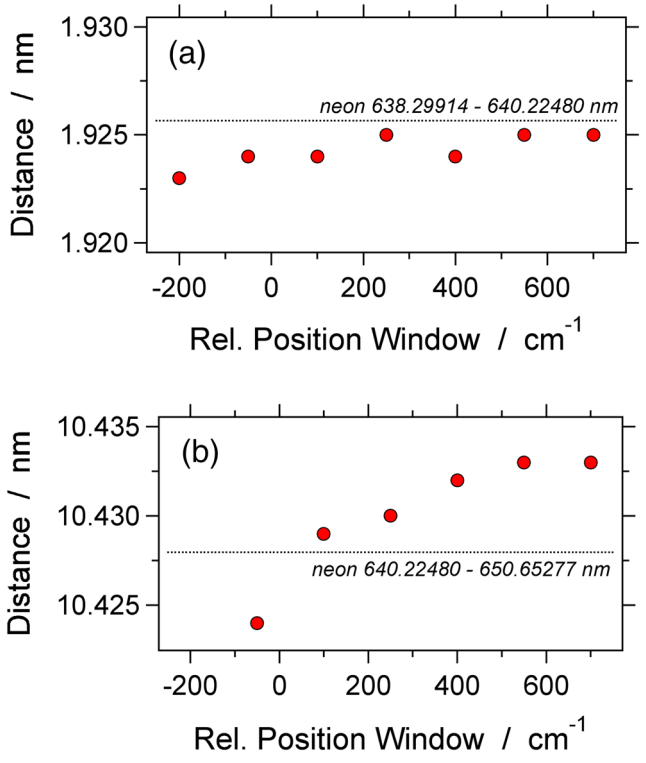


**FIGURE 5** Wavelength distance (in nm) between two neon lines (a) 638.29914 and 640.22480 nm; (b) 640.22480 and 650.65277 nm as a function of the relative peak positions within a single spectral window (0 corresponds to the center position). The dashed lines are theoretical values. The spectra are measured with the LabRAM HR Evolution system, He–Ne laser (632.816 nm), gratings 600 $mm^{-1}$, and a confocal hole 70 μm [Colour figure can be viewed at wileyonlinelibrary.com]

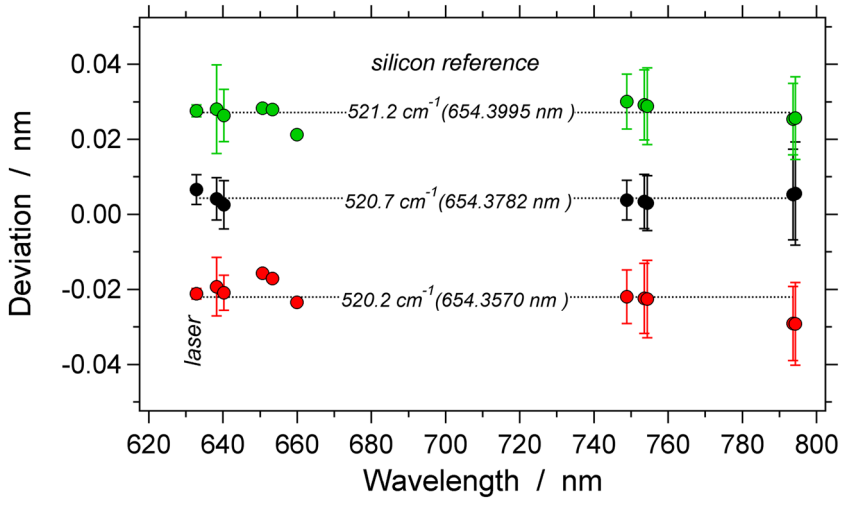


**FIGURE 6** Difference between real wavelengths and calibrated wavelengths of a variety of neon lines between 630 nm and 795 nm according to three different definitions of the silicon Raman band (520.2, 520.7, and 521.2 $cm^{-1}$) that is used for the estimation of the "coeff" parameter in LabSpec. See text for further details [Colour figure can be viewed at wileyonlinelibrary.com]

### 6.6 | Calibration with incorrect laser wavelength

Raman shift of bands expressed in relative wavenumber is directly affected by the wavelength definition of the excitation laser (cf. paragraph 6.3, and paragraph 3 "Laser wavelength uncertainties"). The use of an incorrect definition of the laser wavelength excitation has a major impact on the calibration of Raman bands with neon emission lines. Six different hypothetical laser wavelengths are selected between 532.0 and 532.5 nm to test the reliability of the calibration method (Figure 7). Similar modifications of Raman band and neon line peak positions as described in the preceding paragraph 6.5 are observed. Each selected laser wavelength calibrates the main Raman band of silicon at about 520.7 $cm^{-1}$ (Figure 7a), but this value is obtained by different "coeff" parameters for each laser definition (Figure 7b). The *585* neon line should appear at virtual relative wavenumbers between 1692.592 $cm^{-1}$ and 1710.240 $cm^{-1}$ according to a laser wavelength defined between 532.5 nm and 532.0 nm, respectively (Figure 7c). However, the measured *585* neon line appears at variable wavenumbers between 1705.152 to 1706.335 $cm^{-1}$. The intersection of both trends defines the correct laser wavelength and "coeff" parameter (Figure 7c). In conclusion, Raman bands will be corrected to erroneous lower values if the laser wavelength definition is slightly higher than the true value and to erroneous higher values if the wavelength is slightly lower. A difference of 500 pm in laser wavelength results in a wavenumber shift of approximately 1.18 $cm^{-1}$, whereas a 10 pm difference results in a shift of 0.32 $cm^{-1}$.

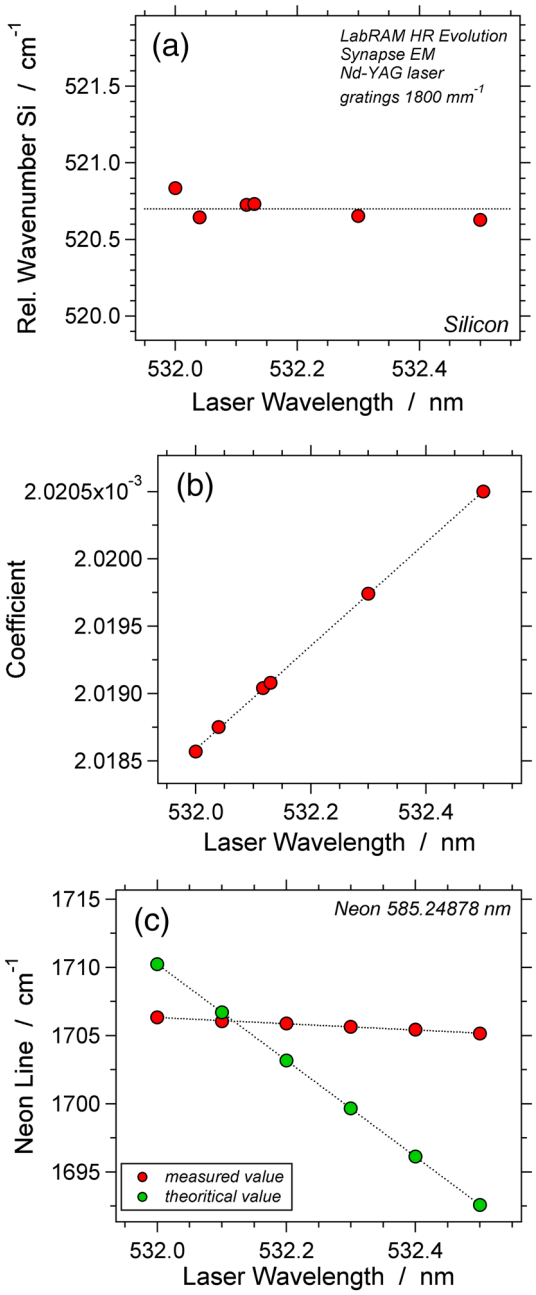


**FIGURE 7** Calibrated wavenumber of silicon using six different definitions of the laser wavelength between 532.0 and 532.5 nm (a). Each calibration corresponds to a specific "coeff" parameter between 0.0020185 and 0.0020205 (b). The virtual relative wavenumber of the *585* neon line reveals significant deviations between measured values and theoretical values (c) [Colour figure can be viewed at wileyonlinelibrary.com]

## 7 | NUMERICAL DATA PROCESSING

The signal that is picked up by photo-diodes of the detector is digitalized and submitted to numerical processes. Delhaya et al.[53] already mentioned that inappropriate digital signal processing methods may yield erroneous and misleading data. An accurate numerical analysis of a spectrum, that is, an estimation of the center position, height, and width of a Raman band, requires that the spectrum be correctly digitized. The necessity of an accurate reproduction of Raman bands is given by its application related to specific physical properties of the investigated material, for example, density of gases. Raman bands in a discontinuous spectrum detected by a pixel array of a specific CCD can be reproduced by a purely mathematical analysis with least-squares fitting procedures using *PDF* (e.g., Yuan and Mayanovic[32]) (Section S2, Supporting Information), such as Gaussian (normal distribution, Figure S1, Supporting Information), Lorentzian (Cauchy distribution, Figure S2, Supporting Information), Voigt (convolution of normal and Cauchy distribution), Gaussian–Lorentzian Sum in addition to many more (e.g., PeakFit v4.12, SYSAT Software Inc.).

These distribution curves are symmetric centered around a peak position. It must be noted that Raman band shapes of gases are often slightly asymmetric and are better reproduced by, for example, an asymmetric Gaussian–Lorentzian distribution, skew normal distribution, or logistic distribution.

Least-squares fitting with *PDF* applied to the intensity of a pixel array results in a shape definition that is characterized by peak position, peak intensity, peak area, and full-width-half-maximum (*FWHM*). It was assumed that a minimum of 3 to 7 pixels is necessary for a correct sampling of the band profile and determination of its shape properties.[53] The band shape is a convolution of the natural Raman band shape and the instrumental response function that may be limited by the resolution of the instrument.[33] The Raman band shape of gases is usually similar to a Lorentzian curve, but the convolution results in a profile intermediate between a Lorentzian and Gaussian profile. Neon lines can also be numerically processed with distribution functions, similar to the analyses of Raman bands, but the line shape resembles a Gaussian distribution. An issue of major importance is the reliability of this reproduction because these lines are often defined by only few pixels. The type of selected *PDF* has a major impact on the shape properties of the modelled band. Occasionally, there may be large variations in intensity, peak position, and width between Gaussian, Lorentzian, Gaussian–Lorentzian, and other functions applied to the same spectrum.

The LabRAM 300 spectrometer reveals the *585* neon line in 6 pixels within a wavenumber range of 16.9 $cm^{-1}$ using a 600 $mm^{-1}$ gratings (Figure 8a). This neon line is positioned at 1707.416 $cm^{-1}$ relative to the laser source (532.08 nm). The limited number of pixels does not allow reliable least-squares fitting of this signal with *PDF*. The three pixels that define the peak position are illustrated in Figure 8b. Lorentzian and Gaussian fittings result in significant different peak positions 1706.978 $cm^{-1}$ and 1706.723 $cm^{-1}$, respectively, and *FWHM* of 6.795 and 5.799 $cm^{-1}$. Relatively small differences between Gaussian and combined Gaussian–Lorentzian fittings illustrate that the line shape is mainly Gaussian. An overview of the intensity deviation of about 20 pixels around the peak position reveals that the Gaussian curve is slightly asymmetric (Figure 8c). Consequently, asymmetric distribution curves such as asymmetric logistic and asymmetric Gaussian–Lorentzian may result in better fits than symmetric *PDF*, that is, higher $R^2$ values. The corresponding peak positions of these asymmetric functions are calculated at significantly higher relative wavenumbers, that is, at 1707.104 and 1708.665 $cm^{-1}$, respectively (Figure 8b). Although the asymmetric Gaussian–Lorentzian curve displays the most accurate fit

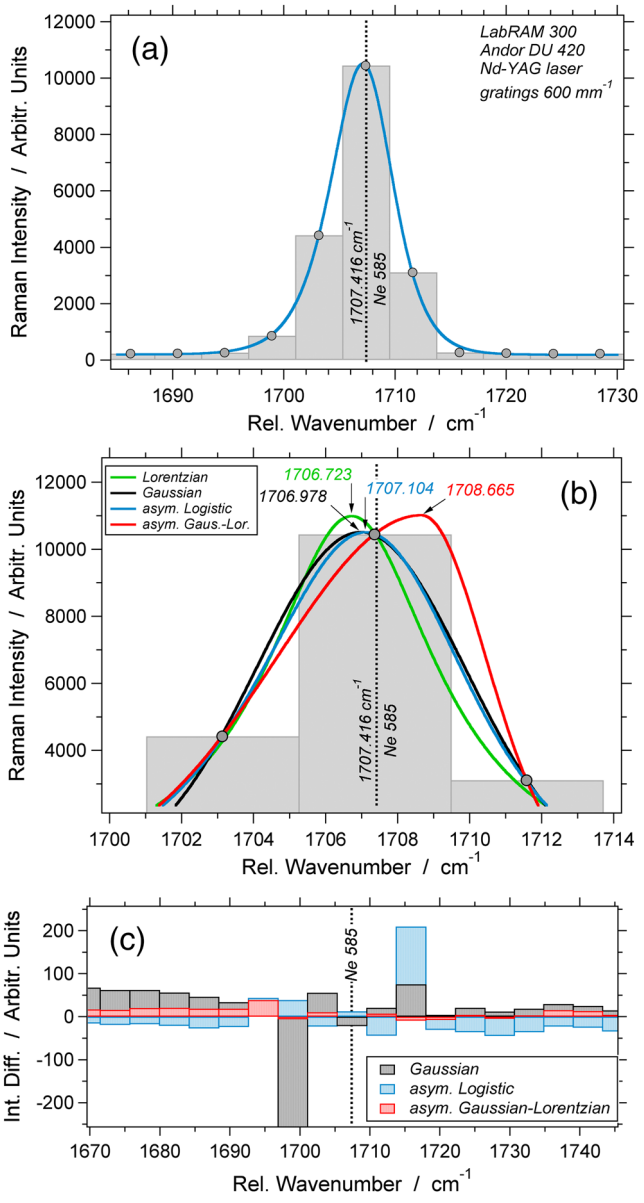


**FIGURE 8** (a) Spectrum of the *585* neon line analyzed with the LabRAM 300 system (600 $mm^{-1}$ gratings), pixel resolution is illustrated by the width of vertical bars, the filled circles are the center position of individual pixels. The blue curve is a least squared best-fit asymmetric logistic distribution function. (b) Various *PDF's* that are fitted to the spectrum illustrated in (a). (c) The difference in intensity between distribution functions and individual pixels of the same spectrum [Colour figure can be viewed at wileyonlinelibrary.com]

to individual intensity values, its shape properties are highly deviating from the expected shape based on the distribution of the three pixels that define the center of the peak area. Using a simple visual estimations, the pixel adjacent to the center at lower wavenumbers is slightly higher than the pixel at higher wavenumbers. Consequently, the true peak value is expected to be

slightly shifted to the left of the central pixel. However, the asymmetric Gaussian–Lorentzian curve defines a peak value to the right. This is a direct consequence of the limited number of pixels that define this peak. The peak fitting procedure in LabSpec splits the asymmetric Gaussian–Lorentzian function in two parts on either side of the peak (Section S2, Supporting Information), which lead to insufficient number of pixels for each side in the fitting procedure. The asymmetric logistic curve is considered the best solution for the reproduction of shape properties of the neon line in this example (Figure 8). It must be noted that the symmetric logistic curve is not suitable for reproducing the shape properties of Raman bands and neon lines. The peak position of a Raman band or neon emission line that is defined by more pixels is less sensitive to the type of *PDF* (Section S7, Supporting Information). This can be obtained by reducing the pixel resolution with a larger line density of the gratings and a larger focal length (Figure S12, Supporting Information). It must be noted that this option may prevent the simultaneous recording of calibration lines, because the size of one spectral window will be largely reduced.

In general, Gaussian distribution curves are the most reliable reproduction of neon lines, and it is only slightly improved by adding a small fraction of Lorentzian properties (up to 5%) and by applying a certain asymmetry. The least-squares fitting procedure also illustrates that the largest deviations between measured and modelled intensities are determined for those pixels that define the center peak position (Figure 8c). Consistent peak position estimations with different *PDF* can only be obtained if the band is defined by at least 12 pixels. Consequently, asymmetric Gaussian–Lorentzian curves need 24 pixels due to splitting in the fitting procedure (Section S2, Supporting Information).

There are abundant disadvantages of numerical data processing, which can be summarized by as follows: (1) different types of *PDF* may result in a large variety of shape properties; (2) the least-squares fitting method is highly biased, dependent on the number of pixels involved in the fitting procedure and the intensity of the background noise (baseline); (3) a calculated distribution curve does not give any information about the uncertainty of individual measurements. Disadvantage 1 can be omitted by using Raman equipment with sufficiently high pixel resolution. The latter (disadvantage 3) is often approached in literature by the repetition of measurements and fitting procedures followed by statistical analyses, that is, the estimation of an average and standard deviation. This is also known as "reproducibility" and is often mistaken for the "uncertainty" in individual measurements (cf. previous studies[24,25]). In conclusion, the shape reproduction with best-fit *PDF* introduces numerous undefined uncertainties in the definition of an accurate gas densimeter.

## 8 | MODIFIED SCANNING MULTICHANNEL TECHNIQUE

Wavelength detection at a subpixel resolution (i.e., within the wavelength range detected by one pixel) is of major importance to gas densimeters. The question may arise can we determine a peak position of Raman bands and emission lines with precisions smaller than the pixel resolution without numerical mathematical manipulations. Sadler et al.[15] introduced the "tilted slit" procedure. Tilting the spectral image across a number of CCD pixel rows enhances the appearance of a spectral line and improves the reconstruction and definition of shape properties, such as peak position at subpixel dimensions. Knoll et al.[13] and Deckert and Kiefer[14] introduced the scanning multichannel technique to analyze the line shape of spectra with higher accuracy. Small step tuning of the gratings rotation, that is, a spectrometer position shift of a quarter of the corresponding spectral width of a single pixel, results in significantly different and improved line shapes. Deckert and Kiefer[14] suggested to combine all spectra of individual positions to reconstruct a recovered line shape, which almost completely reproduced an original Gaussian-like curve. This method is modified and refined in this study to reproduce shape properties of both emission lines of neon and Raman bands of gases such as $CO_2$ and $CH_4$.

The possibility to relocate the gratings in respect to the detector over a distance that is only a fraction of the pixel size offers a method to determine with higher precisions the peak positions of Raman bands and neon emission lines. A hypothetical signal with a peak position at 1700.05 $cm^{-1}$ is illustrated in Figure 9 to elucidate this method. The original band shape (Lorentzian) and the variable positions of the detector with corresponding individual pixels are illustrated in Figure 9a. The relocation is given by positions 1 to 8, where each individual step of the shift is only a fraction of the pixel size. The discontinuous signal picked up by the pixel array in two specific positions is illustrated in Figure 9b,c. The signal in position 1 can be fitted to a Lorentzian curve whereas the signal in position 3 to a Gaussian curve. This example shows that different types of *PDF* with significantly different properties, such as *FWHM* and intensity, can be fitted to the same signal dependent on the position of the detector. A modified method of Deckert and Kiefer[14] is illustrated in Figure 9d, where the line shapes of all

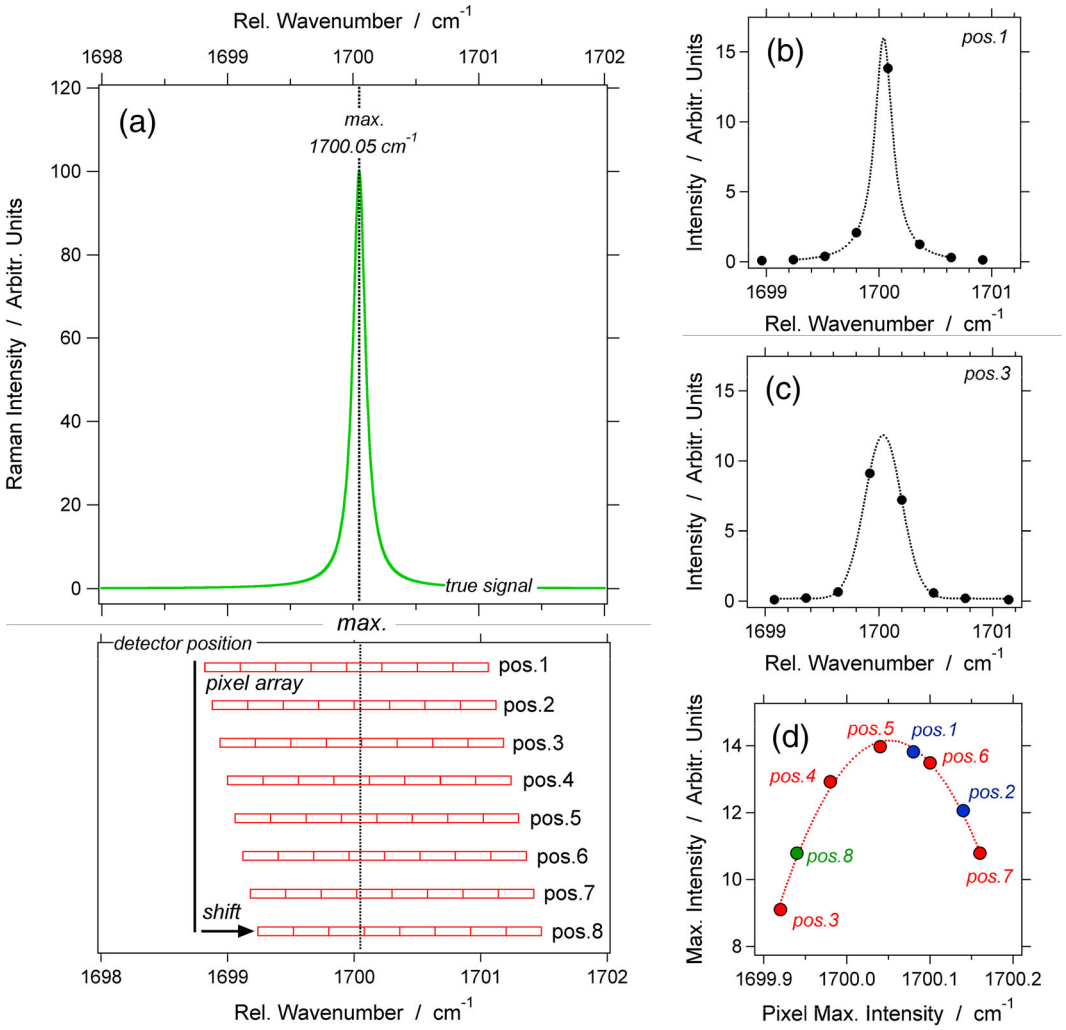


**FIGURE 9** (a) Hypothetical signal of a Raman band or atomic emission line at 1700.05 $cm^{-1}$, with a schematic illustration of the position of a pixel array of the detector; the detected intensity of each pixel in position 1 (b) and position 3 (c) reveal significant different shape properties; (d) accumulated spectrum of the same band plotting only the pixel with the maximum intensity in each position. See text for further details [Colour figure can be viewed at wileyonlinelibrary.com]

spectra are combined in one diagram by plotting the pixel position with the maximum intensity in each step against the absolute value of this intensity. The distribution of these data points may resemble a polynomial function of a second or higher degree, with a maximum at the peak position of the true signal. The density of data points can be increased by more and smaller relocation steps and, thereby, defining with high precision the peak position. This method results in an enhanced precision, defined by the step size of relocation, which is only a fraction of one pixel. However, the uncertainty cannot be exactly determined by this method, but it is assumed to be approximately twice the step size of relocations. A major disadvantage of this method is that it is extremely difficult to maintain the original intensity of the Raman signal constant in a longer time interval to complete the entire set of measurements.

A new procedure that does not require mathematical manipulations and that does not consider the absolute intensity of the signal is illustrated in Figure 10, where the position of the detector (in nm) is plotted against the position of the pixel with the highest intensity. Figure 10a reveals a detail of Figure 9a, where the maximum intensity is relocated to an adjacent pixel (from positions 2 to 3). The center between both positions (pixels B and C) is an accurate approach of the true peak position (best estimate). The uncertainty in this center position is the wavelength overlap of the two pixels, which is the step size of the shift. It must be noted that the step size is equal to the value of the "coeff" parameter, which is defined by the calibration procedure of the LabRAM system (Section S3 in Supporting Information). Each pixel goes through a cycle upon the rotation of the gratings (Figure 10b). A complete cycle is illustrated for

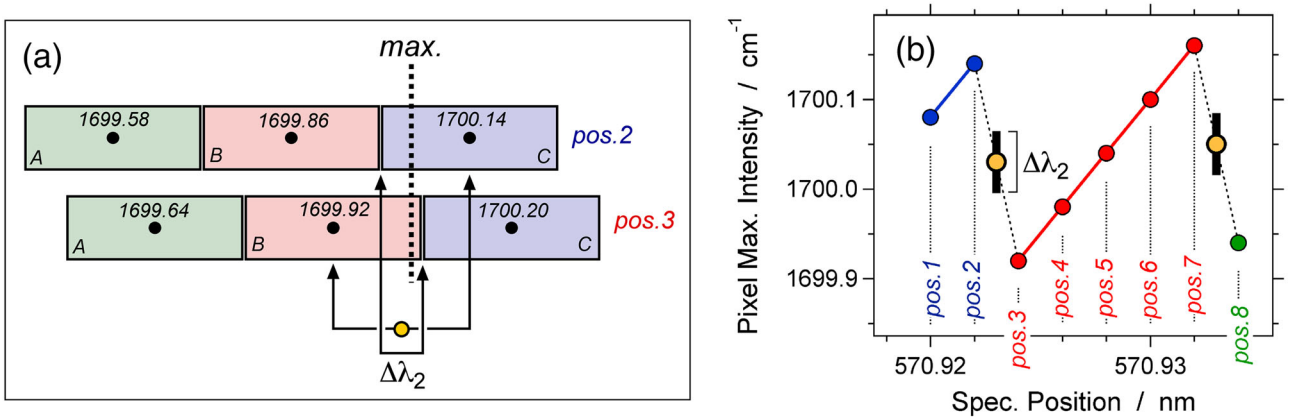


**FIGURE 10** (a) Detail of Figure 9a illustrating the shift of three pixels (*A*, *B*, and *C*) and the position of the maximum intensity of the Raman signal. The transition from positions 2 to 3 is used to calculate the peak position of the Raman band (yellow filled circle), and the overlap of both pixels defines the uncertainty ($\Delta\lambda_2$). (b) Accumulated data of the position of pixels with maximum intensity versus the position of the spectrometer (shift numbers). The black bar illustrates the uncertainty $\Delta\lambda_2$. See text for further details [Colour figure can be viewed at wileyonlinelibrary.com]

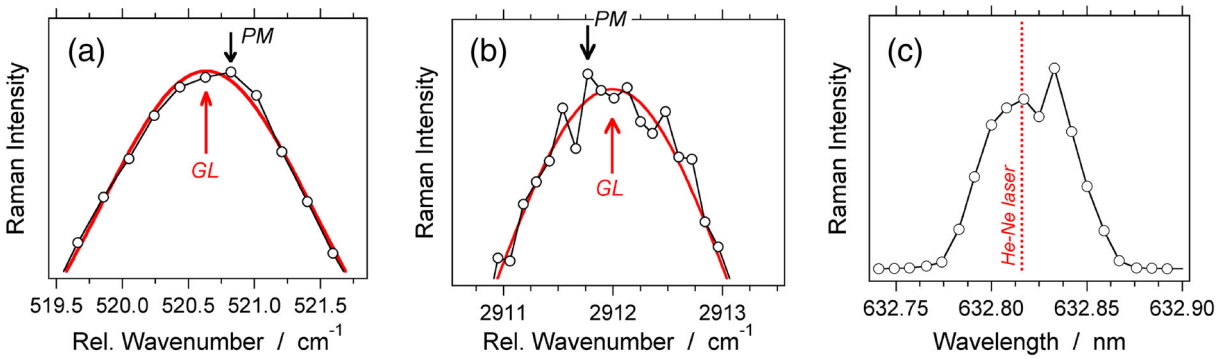


**FIGURE 11** Examples of irregularities in the Raman spectra of silicon (a), methane (b), and the Rayleigh scatter of the He–Ne laser (c) near the peak positions. *PM* is the pixel with the maximum intensity, *GL* is the peak position of a Gaussian–Lorentzian best-fit distribution curve defined by a relative short range of pixels centered around this peak [Colour figure can be viewed at wileyonlinelibrary.com]

pixel B (positions 3 to 7). The peak position of the true signal is determined by the average between two cycles at the transition.

The estimation of a pixel with the maximum intensity may be troubled by intensity irregularities of the detection method. The intensity of individual pixels of Raman bands and neon lines may deviate significantly from a smooth Gaussian–Lorentzian distribution curve. These so-called outlier pixel (e.g., Hutsebaut et al.[29]) may inhibit proper analyses with distribution curves and the accurate determination of peak positions of Raman bands and neon lines. The outlier may occur systematically (Figure 11a,c) and randomly (Figure 11b). These effects can be assigned to response nonuniformity of the detector, dark current nonuniformity of individual pixels (i.e., the fixed pattern noise), and residual charges.[54] Whereas cosmic ray effects are automatically corrected in LabSpec software, other nonuniformities remain within the collected spectra. Outlier pixels in Figure 11a,c may occur due to irregular reflections of the edge filter, which is caused by different incident angles of the laser beam. This effect can be reduced by decreasing the size of the confocal hole. A fixed pattern noise may affect a Raman band (Figure 11b). This signal can be improved by multiple measurements of the same spectrum using the accumulation procedure in LabSPEC. Occasionally, this effect cannot be reduced, and hypothetical pixel positions with maximum intensity must be determined with polynomial functions or *PDF* in the relatively small wavelength range of the supposed peak.

## 9 | CASE STUDY 1: WANDERING NEON EMISSION LINES

The effects of grating rotation on peak position estimation with the modified scanning multichannel technique (*SMT*, see preceding paragraph 8) and the generally accepted least-squares fitting with *PDF's*, that is, symmetric and asymmetric Gaussian–Lorentzian curves, are investigated with several neon lines (Figure 12). The example in Figure 12a illustrates the estimation of peak position of the *567* neon line. The minimum step size of the gratings rotation is about 0.004 nm with the LabRAM 300 system (Nd–YAG laser, 532.08 nm, 1800 $mm^{-1}$ gratings), corresponding to about 0.14 $cm^{-1}$. For comparison, the "coeff" parameter in LabSpec is estimated with the reference Raman band of silicon at 0.00429039. The *SMT* involves about 10 to 12 steps within one cycle according to a pixel resolution of 1.377 $cm^{-1}$ (cf. Figure 10b). The relative wavenumber of the pixel with the maximum intensity of the virtual *576* neon line varies between 1445.83 $cm^{-1}$ and 1447.24 $cm^{-1}$ according to the position of the spectral window. The transition between the cycles defines the peak position of this neon line at 1446.548 ± 0.064 $cm^{-1}$ at a spectral window position of 557.298 nm (Figure 12a). The uncertainty is defined by the wavelength overlap of the two pixels at the transitions (cf. Figure 10). The peak position is modified to 1446.453 ± 0.064 $cm^{-1}$ and 1446.61 ± 0.063 $cm^{-1}$ in the following cycles, which illustrates only a minor shift within the limits of the uncertainty. In addition, the center positions of symmetric Gaussian–Lorentzian curves are estimated for each spectrum in every relocation step (Figure 12a). This peak position appears in a wavy pattern that is slightly shifted to higher wavenumbers at higher spectral window positions. The peak position at the transition position is within the uncertainty range estimated with *SMT*, that is, at the lower end of the error bars in Figure 12a. The wavy pattern of the asymmetric Gaussian–Lorentzian curve illustrates a larger variation, which is caused by the increased variability due to the limited number of pixels that are involved in asymmetric fitting procedure (cf. Figure 8).

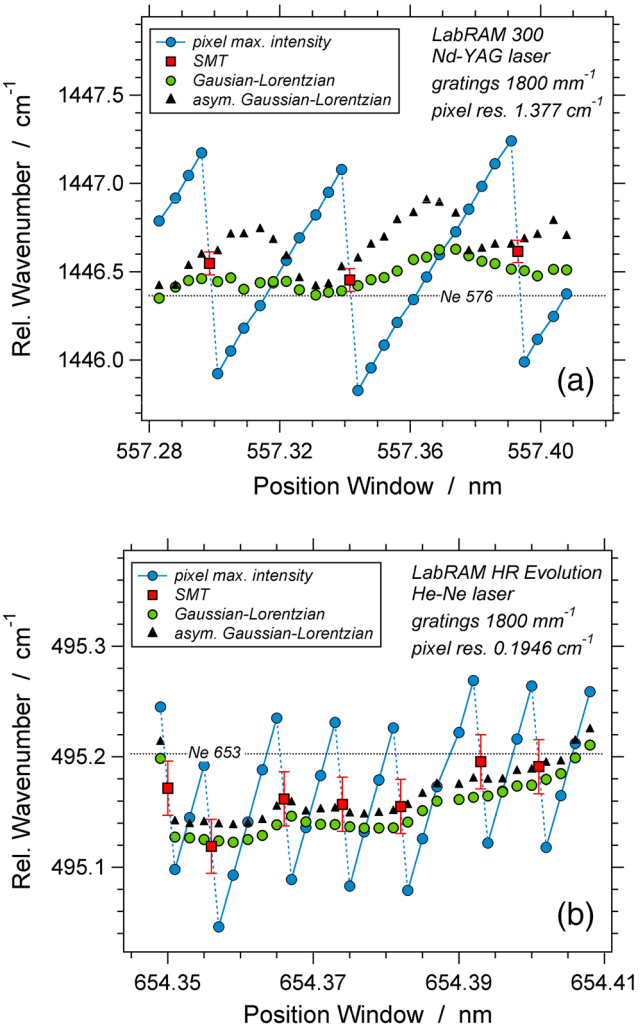


**FIGURE 12** Relative wavenumber of the peak position of the *576* neon line (a) and the *653* neon line (b) as a function spectral window position analyzed with the different Raman systems as illustrated in the image. See text for further details [Colour figure can be viewed at wileyonlinelibrary.com]

A similar experiment is performed with the LabRAM HR Evolution system using a He–Ne laser (632.816 nm, Figure 12b) and a Nd–YAG laser (see Section S8 in Supporting Information). The peak position of the *653* neon line is analyzed with *SMT* in addition to symmetric and asymmetric Gaussian–Lorentzian distribution curves (Figure 12b). The minimum step size of the gratings rotation is about 0.002 nm (0.047 $cm^{-1}$), and only about four to five steps are included in one cycle, due to a pixel resolution of 0.1946 $cm^{-1}$. The *SMT* peak positions vary between 495.119 ± 0.024 $cm^{-1}$ and 495.196 ± 0.024 $cm^{-1}$, which illustrates a significant shift to higher values that exceeds the individual uncertainties (Figure 12b). The same trend is illustrated with symmetric and asymmetric Gaussian–Lorentzian best-fit curves (Figure 12b) that reveal a gently wavy appearance. These peak positions are within the uncertainty limits determined by *SMT* at transition positions, both towards the upper and lower end of the error bars. An irregular discontinuity occurs at the transition between 654.349 and 654.351 nm where the virtual relative wavenumber of the peak position reveals a sudden decrease from 495.245 to 495.09 $cm^{-1}$, most probably due to irregularities of mechanical properties of the Sinus Arm Drive.

In conclusion, the peak position of neon lines in a specific window is highly dependent on its position, that is, the amount of rotation of the gratings directly related

to the Sinus Arm Drive properties, but the variability remains within one to two pixels of the detector. *SMT* is able to define an uncertainty in individual measurements at subpixel dimensions, however, only at the transition positions between two cycles. It is assumed that this uncertainty is also valid to peak position estimations within one cycle between the transitions. The application of only distribution curves to define peak positions must consider this uncertainty in individual measurements of Raman bands and neon lines. A generalized uncertainty of best-fit *PDF* is estimated at twice the value obtained by *SMT*, because these peak positions are detected at upper and lower limits of the *SMT* uncertainty. The uncertainty is about 0.1 $cm^{-1}$ for the LabRAM HR Evolution system using the 1800 $mm^{-1}$ gratings and about 0.2 $cm^{-1}$ using the 600 $mm^{-1}$ gratings. Center positions of *PDF* of spectra obtained with the LabRAM 300 system (1800 $mm^{-1}$ gratings) have an uncertainty of about 0.22 $cm^{-1}$. The uncertainty of the LabRAM 300 is comparable with the LabRAM HR Evolution because both systems reveal a similar minimum step sizes of the gratings rotation, despite the much larger pixel resolution of the LabRAM HR Evolution system.

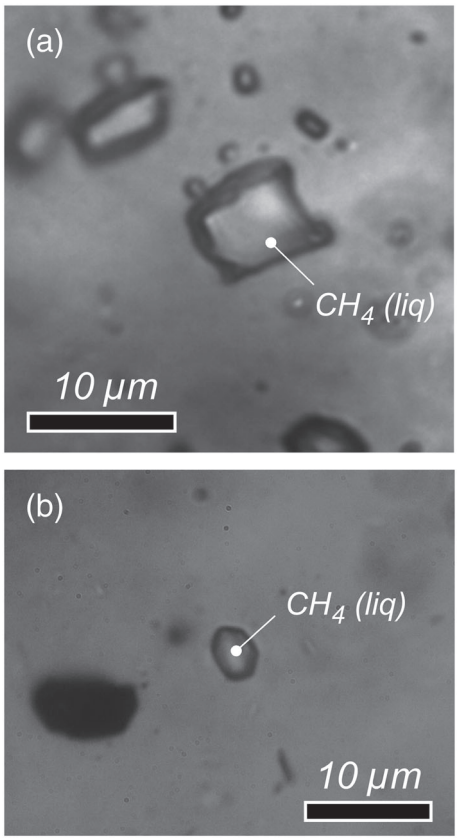


**FIGURE 13** Photomicrographs of two natural $CH_4$ fluid inclusions in quartz with a density of 0.3461 ± 0.0002 g·$cm^{-3}$ (a) and 0.4011 ± 0.0001 g·$cm^{-3}$ (b)

## 10 | CASE STUDY 2: METHANE

The main Raman band of $CH_4$ (C–H symmetric stretching band $\nu_1$) has a variable peak position, approximately from 2910 to 2918 $cm^{-1}$ dependent on its fluid density (precious works[1,4,18,20,44] and references therein). Natural $CH_4$ fluid inclusions (Figure 13) are selected to test the analytical method described in the present study with the different Raman systems (see Table 1). The fluid inclusions are hosted in quartz within garnetites that were metamorphosed at highly reducing granulite-facies conditions.[55] The density of the two examples is determined with microthermometry at 0.3461 ± 0.0002 g·$cm^{-3}$ (46.35 ± 0.03 $cm^3$·$mol^{-1}$, Figure 13a) and 0.4011 ± 0.0001 g·$cm^{-3}$ (40.00 ± 0.02 $cm^3$·$mol^{-1}$, Figure 13b), calculated with the equation of state of Setzmann and Wagner[9] that is adapted to fluid inclusion research in the software package *FLUIDS* (https://fluids.unileoben.ac.at).[56] The $CH_4$ spectra resemble a Lorentzian distribution curve and is defined within the range 2895 to 2925 $cm^{-1}$ (Figure 14). This range corresponds to about 30 pixels with the LabRAM 300 (1800 $mm^{-1}$ gratings, Nd–YAG laser, Andor DU detector), 60 pixels with the LabRAM HR Evolution (600 $mm^{-1}$ gratings, He–Ne laser, Synapse EM detector), and 150 pixels with the LabRAM HR Evolution (1800 $mm^{-1}$ gratings, Nd–YAG laser, Synapse EM detector). The $CH_4$ spectra are recorded simultaneously with the nearby *753*, *754*, and *794* neon lines using a He–Ne laser source (Figure 14a) and the *626*, *630*, and *633* neon lines using a Nd–YAG laser source (Figure 14b). The wavelength span detected within a spectral window with the LabRAM HR Evolution, 1800 $mm^{-1}$ gratings, and a He–Ne laser source (e.g., 2818–3006 $cm^{-1}$) does not include any reference neon lines for calibration and, therefore, cannot be used to determine accurate values of $CH_4$ peak positions. Moreover, the use of narrower gratings, for example, 2400 $mm^{-1}$, increases the pixel resolution, but the accuracy cannot be determined due to the absence of reference emission lines within a single spectral window. $CH_4$ peak position is calibrated with *SMT* and with best-fit *PDF's* (Figure 15). A similar pattern as observed with neon emission lines (cf. Figure 12) is illustrated in Figure 15: a gently wavy appearance of symmetrical and asymmetrical Gaussian–Lorentzian best-fit curves and a continuous decrease (Figure 15a) or increase (Figure 15b) at higher spectral window positions. The best-fit *PDF's* define similar peak positions as *SMT* at transition positions and remain within the uncertainty range of *SMT*; that is, peak positions occur at both the lower and upper limit of the *SMT* uncertainty. The

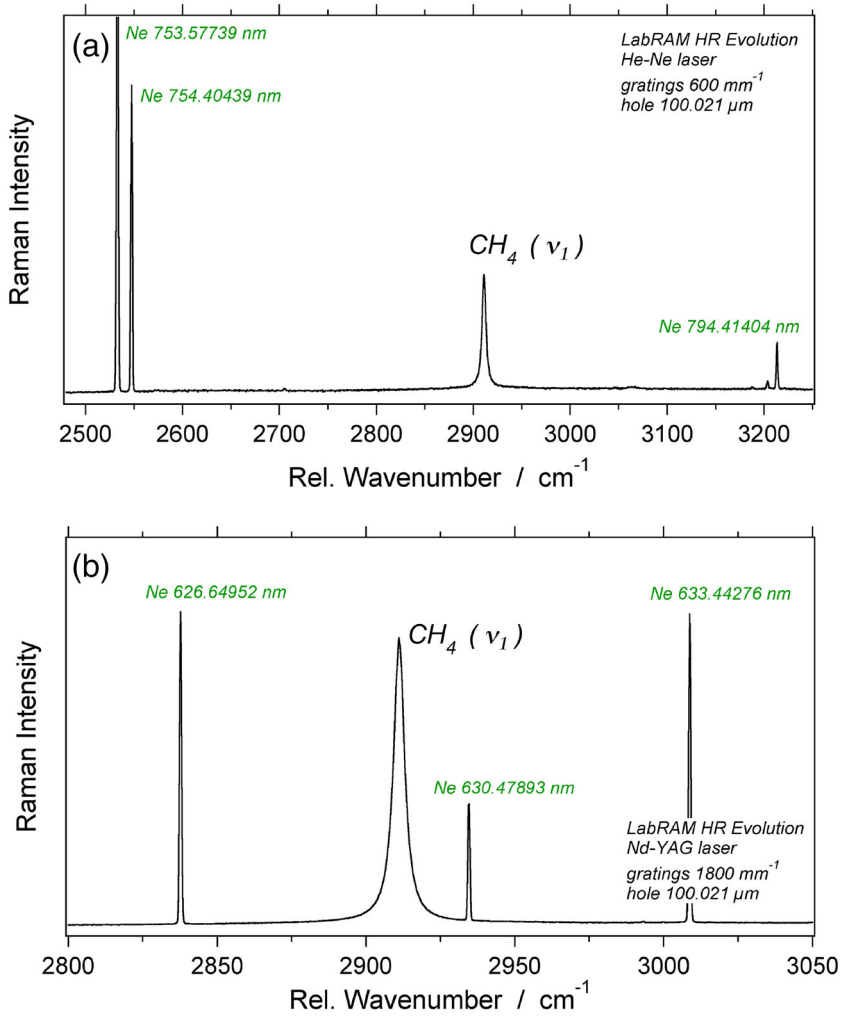


**FIGURE 14** Raman spectra of $CH_4$ with simultaneously recorded neon lines with the LabRAM HR Evolution system, using a He–Ne laser (a) and a Nd–YAG laser (b) [Colour figure can be viewed at wileyonlinelibrary.com]

uncertainty of peak position estimations based on only distribution curve fittings is, therefore, twice the value determined with *SMT*.

The $CH_4$ peak of the 0.3461 g·cm$^{-3}$ fluid inclusion (Figure 13a) is calibrated with the proper bracketing technique using three reference neon emission lines: *753*, *754*, and *794* (see paragraph 6.2), analyzed with the LabRAM HR Evolution system, 600 mm$^{-1}$ gratings and a He–Ne laser (Figures 14a and 15a). Best-fit Gaussian–Lorentzian distribution curves of neon lines are used in the calibration procedure to design a linear best-fit trendline through neon peak positions. The position of $CH_4$ is interpolated according to this line. The average and standard deviation of the $CH_4$ peak positions in 25 different spectral windows that are relocated according to the smallest step size of the gratings rotation (Figure 15c) is 775.691 ± 0.001 nm (LabRAM HR Evolution, He–Ne laser, 600 mm$^{-1}$ gratings), corresponding to 2910.66 ± 0.02 cm$^{-1}$. It must be noted that this standard deviation is not reflecting the uncertainty of individual measurement. The original gently wavy appearance and peak shift (Figure 15a,b) is absent for calibrated values of $CH_4$ in Figure 15c, because both neon lines and the Raman band are equally affected by the gratings relocation. However, the uncertainty in individual measurements defined by *SMT* is ± 0.007 nm, which finally corresponds to a wavenumber of 2910.66 ± 0.12 cm$^{-1}$. This value is not significantly different from 775.686 ± 0.007 nm (2910.57 ± 0.12 cm$^{-1}$) of the other $CH_4$ fluid inclusion with a density of 0.4011 g·cm$^{-3}$ (Figure 13b). The inferred uncertainty for best-fit *PDF's* is 0.24 cm$^{-1}$, that is, about half the size of a pixel (i.e., 0.52 to 0.55 cm$^{-1}$).

Raman analyses with a Nd–YAG laser result in a larger variety of wavenumbers of the same $CH_4$ fluid inclusions, which is mainly caused by the inaccurate definition and variability of the laser wavelength. Similar to He–Ne lasers, $CH_4$ peaks are calibrated with the proper bracketing technique using three reference neon emission lines: *626*, *630*, and *633* (Figure 14b). The 0.4011 g·cm$^{-3}$ $CH_4$ inclusion (Figure 13b) is calibrated at an average value of 629.545 nm (LabRAM HR Evolution, Nd–YAG laser 532.04 nm, 1800 mm$^{-1}$ gratings). According to *SMT* uncertainty, the corresponding

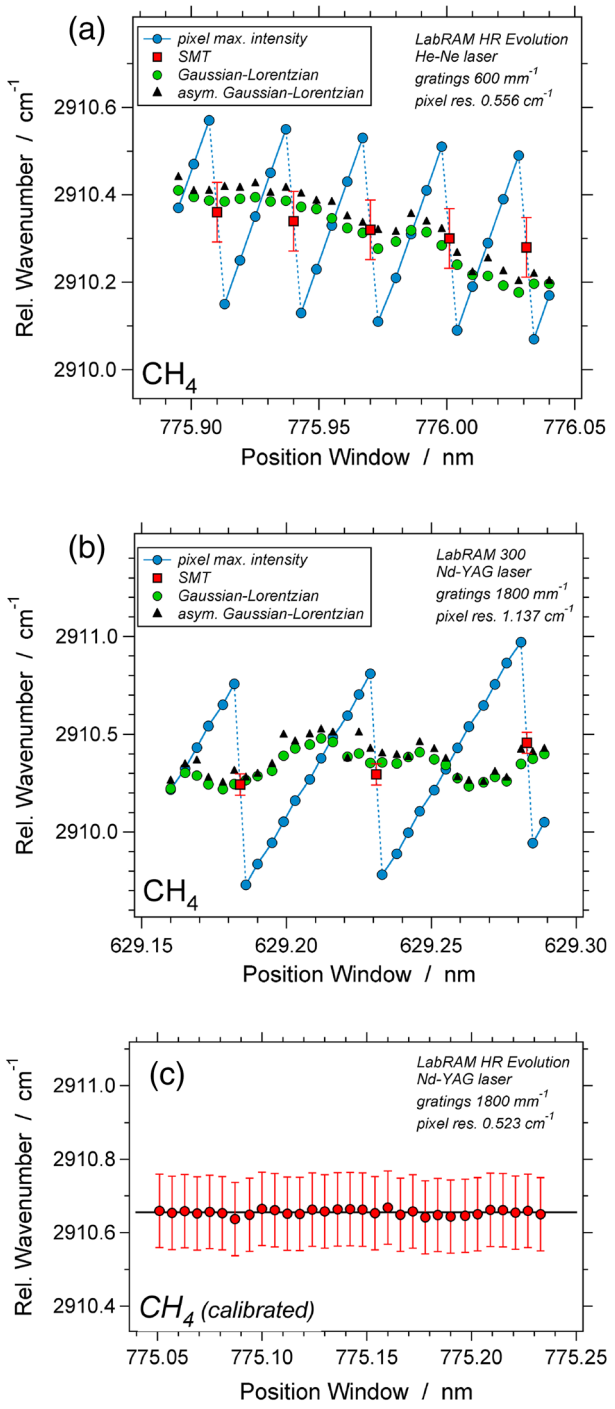


**FIGURE 15** (a) Relative wavenumber of the peak position of $CH_4$ as a function of spectral window position, estimated with *SMT* and symmetric and asymmetric Gaussian–Lorentzian curves using the LabRAM HR Evolution system with He–Ne laser; (b) similar image using the LabRAM 300 system with a Nd–YAG laser. (c) Calibrated relative wavenumber of peak positions of $CH_4$ as a function of spectral window position, using the proper bracketing method with three adjacent neon lines. All peak positions are obtained with best-fit Gaussian–Lorentzian curves. The error bars illustrate the uncertainty estimated with *SMT* [Colour figure can be viewed at wileyonlinelibrary.com]

wavenumber is $2911.09 \pm 0.05\ cm^{-1}$. This relative wavenumber is inconsistent with the previously determined value using a He–Ne laser. However, similar peak positions are obtained with a hypothetical Nd–YAG laser wavelength definition of 532.055 nm, which is well within possible variations caused by ambient conditions. The laser wavelength was not adequately determined before the measurement session and may have been modified during the session. As illustrated in the preceding paragraph, irregularities in the mechanical rotation of the gratings (Sinus Arm Drive) may also be a cause of inconsistencies in calibrated wavelength values. Analyses of the same fluid inclusion with the LabRAM 300 ($1800\ mm^{-1}$ gratings) and a well-calibrated wavelength of the Nd–YAG laser (532.064 nm) result in a calibrated $CH_4$ wavenumber of $2910.50 \pm 0.13\ cm^{-1}$, which is consistent with the previously determined values. The uncertainty is similar to the value obtained for the LabRAM HR Evolution system using a He–Ne laser and a $600\ mm^{-1}$ gratings, despite a much larger pixel resolution of about $1.14\ cm^{-1}$. This example illustrates that the uncertainty is mainly defined by the minimum rotation step of the gratings (approximately 0.004 nm). Calibration procedures may result in a similar accuracy of Raman band peak positions despite the differences in focal length (300 versus 800 mm) and pixel resolution. Furthermore, this example illustrates that different Raman systems reproduce consistent relative wavenumbers of $CH_4$ in the same fluid inclusion. The inconsistencies of data sets published in literature are further discussed in Section S9 (Supporting Information).

## 11 | CASE STUDY 3: CARBON DIOXIDE

The main Raman bands of $CO_2$ are affected by density, pressure, and temperature and are documented by a number of studies.[2,4,7,22,28,34,37,40,41,43,47,48,50] The effect of temperature was not considered in the earlier studies (before 2012), and spectra were only described with density equations. Bakker[57] emphasized the necessity to describe a homogeneous $CO_2$ phase with at least two intensive variables, according to the limitations of a one-component system (Gibbs phase rule). For example, the density of pure $CO_2$ is defined by temperature and pressure[8] or alternatively by temperature and Raman band wavenumbers. Successive studies (after 2017) provide various equations that describe $CO_2$ density and pressure as a function of temperature and Fermi dyad wavenumbers. However, most of these studies provide inconsistent experimental data sets and inconsistent mathematical equations.

A set of synthetic fluid inclusions (Figure 16) are analyzed according to the method described in the preceding paragraphs, mainly to define the uncertainty in individual measurements of Raman bands. These inclusion are also used to test the accuracy and reliability of earlier published equations that were designed as $CO_2$ densimeter. $H_2O$–$CO_2$-rich fluid inclusions were synthesized at the Utrecht University[58] and Montanuniversity Leoben, according to the method described in Bakker.[59] The calculated densities of $CO_2$ in the fluid inclusions are 0.1477 ± 0.0006 g·cm$^{-3}$ (298 ± 1 cm$^3$·mol$^{-1}$, Figure 16a) and 0.8880 ± 0.0007 g·cm$^{-3}$ (49.56 ± 0.03 cm$^3$·mol$^{-1}$, Figure 16b). Details of the calculation procedures with microthermometrical data are given in Section S10 (Supporting Information).

The $CO_2$ Raman spectrum contains at least five bands in the range 1250 to 1420 cm$^{-1}$ (Figure 17) that can be detected with the different Raman: Fermi dyad (lower and upper band), two "hot bands," and an isotopical modification of the Fermi dyad ($^{13}CO_2$, only the upper band).[60,61,62] The $CO_2$ bands can be calibrated with a variety of adjacent neon lines. The *565*, *568*, *571*, *574*, and *576* neon lines are used in a Raman system with a Nd–YAG laser (Figure 17a), whereas the *667*, *671*, *692*, *702*, and *703* neon lines are used with a He–Ne laser (Figure 17b). The *692* neon line coincides with the $^{13}CO_2$ band, whose shape may be therefore slightly distorted. These lines can be detected simultaneously with $CO_2$ bands within a single spectral window. High resolution analyses with the LabRAM HR Evolution system using an 1800 or 2400 mm$^{-1}$ gratings and a He–Ne laser do not allow accurate calibration possibilities because most of these reference neon lines cannot be detected in a single spectral window with the $CO_2$ bands. The lower and upper band shape of $CO_2$ can be reproduced with best-fit symmetrical Gaussian–Lorentzian distribution curves. The lower band resembles an approximately 12% Gaussian curve (88% Lorentzian) and the upper band a 23% Gaussian curve (77% Lorentzian) in spectra collected with the Synapse EM detector in the LabRAM HR Evolution system. The bands resemble a 35% and 50% Gaussian curve with the Syncerity OE detector, respectively.

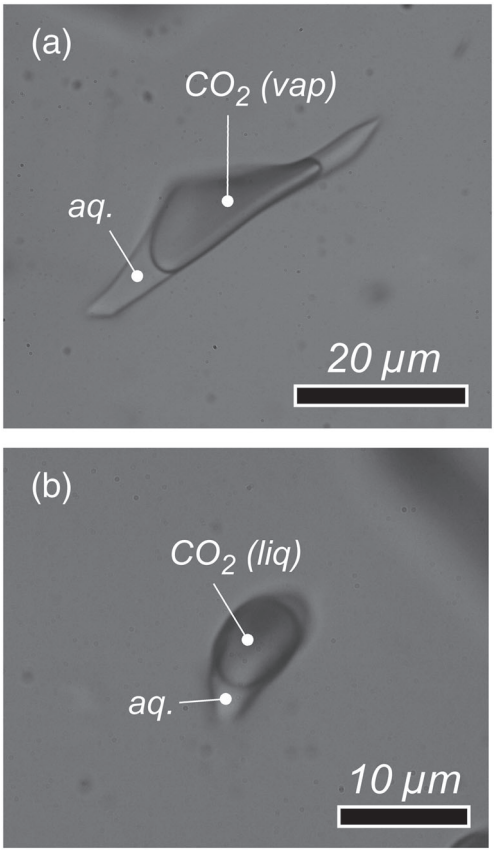


**FIGURE 16** Photomicrographs of two synthetic $CO_2$-rich fluid inclusions in quartz with a density of 0.1477 ± 0.0006 g·cm$^{-3}$ (a) and 0.8880 ± 0.0007 g·cm$^{-3}$ (b). The walls of the inclusions are wetted with an aqueous solution (*aq*)

The calibrated values of $CO_2$ Raman bands according to the proper bracketing method including five neon lines (cf. paragraph 6.2) are illustrated in Table 2. The peak positions of the lower and upper $CO_2$ band and the Fermi dyad distance are revealed in absolute wavelengths (Table 2a) and in relative wavenumbers (Table 2b). Whereas absolute wavelengths are highly variable according to the excitation laser wavelength, relative wavenumbers are approximately similar. The "range" in Table 2 illustrates the spread of calibrated values according to the number of spectral windows, usually in the range of 20 to 30, and the "uncertainty" is defined by *SMT*. The total uncertainty over the entire range of spectral window positions is the sum of both (upper-lower bounds method). Peak positions of individual Raman bands reveal significant difference between different settings of the Raman systems. However, the Fermi dyad distance analyses are consistent for both fluid inclusions (cf. Fall et al.[41]). The average Fermi dyad of the 0.1477 g·cm$^{-3}$ fluid inclusion is 103.12 cm$^{-1}$ (Table 2b), with an uncertainty of ±0.26 cm$^{-1}$. Notice that this uncertainty is by definition the sum of uncertainties of the upper and lower bands of $CO_2$. The 0.8880 g·cm$^{-3}$ fluid inclusion has a Fermi dyad of 104.71 cm$^{-1}$ with an uncertainty of ±0.26 cm$^{-1}$. The inconsistencies of data sets published in literature are further discussed in Section S11 (Supporting Information).

An example of the calibration procedure is illustrated in Figure 18. Gratings rotation according to the minimum step-size results in a systematic shift of the detector pixel with the maximum intensity (*SMT*), illustrating 5 cycles in Figure 18a. The transition between the cycles defines the position of the peak value and its uncertainty

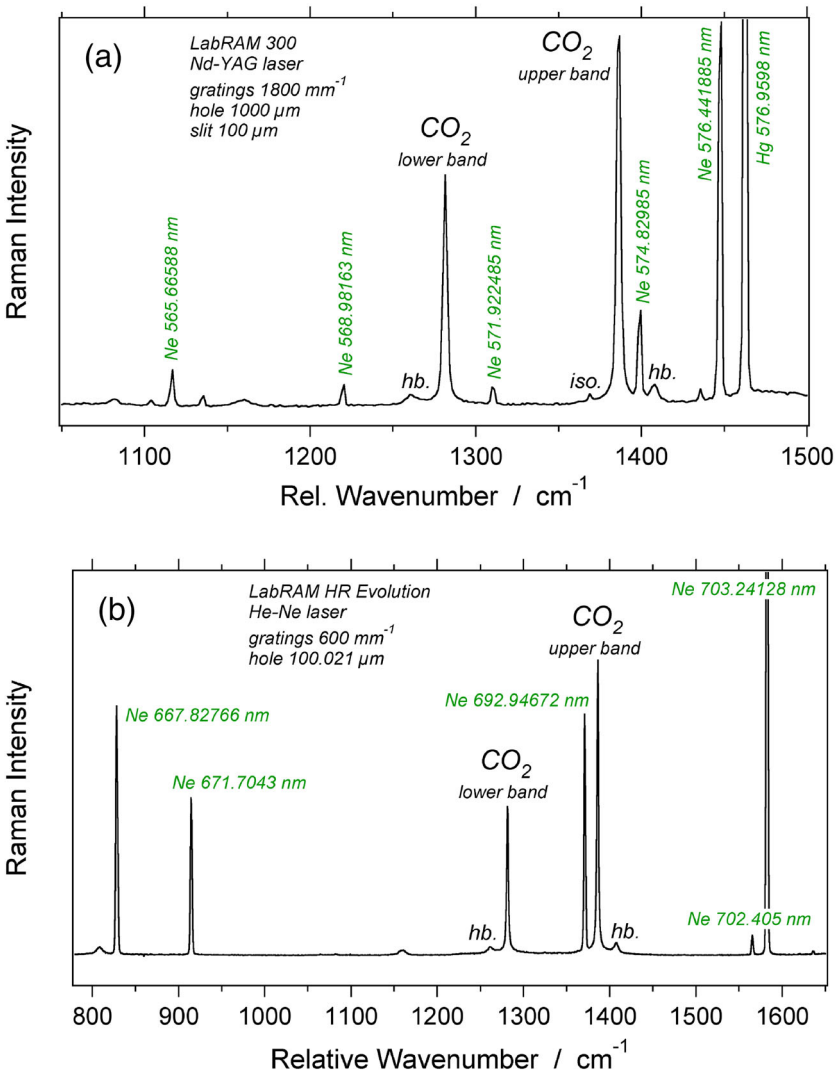


**FIGURE 17** Raman spectra of $CO_2$ with simultaneously recorded neon lines analyzed with the LabRAM 300 system, Nd–YAG laser (a), and the LabRAM HR Evolution system, He–Ne laser (b) [Colour figure can be viewed at wileyonlinelibrary.com]

(*SMT* ±0.066 $cm^{-1}$). However, the peak position is significantly shifted with increasing gratings rotation (i.e., irregularities of the Sinus Arm Drive). This shift is also visualized with best-fit Gaussian-Lorentzian curves. The calibrated peak position of the lower $CO_2$ band according to Gaussian-Lorentzian best-fit values is systematically shifted to lower values at higher rotation angles of the gratings (Figure 18b). The uncertainty in these values (±0.131 $cm^{-1}$) is approximately twice the value of *SMT*. Figure 18a illustrates that *PDF* peak positions occur within the error range of *SMT*. The calibrated peak value of the lower $CO_2$ band is therefore dependent on the spectral window position, which is the main cause of the differences illustrated in Table 2b. The variation in Figure 18b is within the uncertainty estimations of each individual measurement. The upper $CO_2$ band is affected in a similar way by relocation of the gratings, and consequently the Fermi dyad (i.e., the wavenumber difference between the upper and lower band) remains at a nearly constant value (Figure 18c), with an uncertainty of ±0.262 $cm^{-1}$. Both Raman systems, LabRAM 300 and LabRAM HR Evolution reveal similar uncertainties in terms of wavenumber using a 1800 $mm^{-1}$ gratings (Nd–YAG laser) and a 600 $mm^{-1}$ gratings (He–Ne laser), respectively.

The various calibration methods (paragraph 6.1 and 6.2) are tested with the 0.1477 $g{\cdot}cm^{-3}$ fluid inclusion (Figure 16a). The non-linearity of the spectrometer is illustrated in Figure 19, using a $CO_2$ spectrum collected with the LabRAM HR Evolution system, Nd–YAG laser and 1800 $mm^{-1}$ gratings. The pixel resolution is approximately 8.9 pm (0.273 $cm^{-1}$) at the position of the $CO_2$ peaks. Five neon lines are recorded simultaneously with the $CO_2$ signal, that is, *565*, *568*, *571*, *574*, and *576*. The difference between theoretical values and best-fit Gaussian-Lorentzian peak positions of neon lines is not constant in the selected spectral window position, and varies systematically from lower to higher values at higher wavelengths (Figure 19). Seven possible calibration procedures are considered to estimate the

**TABLE 2a** Peak position estimates (wavelength, nm) of calibrated $CO_2$ spectra of the inclusions illustrated in Figure 16

| Fluid inclusion density | Laser | Gratings | Focal length | Pixel res.* | $CO_2$ (lower band) | | | $CO_2$ (upper band) | | | Fermi dyad | | |
|---|---|---|---|---|---|---|---|---|---|---|---|---|---|
| | | | | | Peak | Range | Uncertainty | Peak | Range | Uncertainty | Distance | Range | Uncertainty |
| g/cm$^3$ | nm | mm$^{-1}$ | mm | pm | nm | pm | pm | nm | pm | pm | nm | pm | pm |
| 0.1477 | 532.04 | 1800 | 800 | 8.9 | 571.0882 | ±0.5 | ±2.0 | 574.4712 | ±0.4 | ±2.0 | 3.3829 | ±0.4 | ±4.0 |
| | 632.816 | 600 | 800 | 31.8 | 688.8054 | ±2.2 | ±6.2 | 693.7331 | ±3.0 | ±6.2 | 4.9277 | ±1.2 | ±12.4 |
| | 532.02 | 1800 | 300 | 46.2 | 571.1070 | ±6.0 | ±4.2 | 574.4901 | ±5.0 | ±4.2 | 3.3831 | ±4.0 | ±8.4 |
| | 632.817 | 600 | 800 | 51.7 | 688.8300 | ±1.4 | ±6.0 | 693.7585 | ±1.4 | ±6.0 | 4.9285 | ±1.1 | ±12.0 |
| 0.8880 | 532.02 | 1800 | 300 | 46.2 | 570.9861 | ±2.7 | ±4.2 | 574.4203 | ±2.0 | ±4.2 | 3.4342 | ±2.3 | ±8.4 |
| | 632.816 | 600 | 800 | 31.8 | 688.6673 | ±3.5 | ±6.2 | 693.6693 | ±3.3 | ±6.2 | 5.0020 | ±0.5 | ±12.4 |

**TABLE 2b** Peak position estimates (relative wavenumber, cm$^{-1}$) of calibrated $CO_2$ spectra of the inclusions illustrated in Figure 16

| Fluid inclusion density | Laser | Gratings | Focal length | Pixel res.* | $CO_2$ (lower band) | | | $CO_2$ (upper band) | | | Fermi dyad | | |
|---|---|---|---|---|---|---|---|---|---|---|---|---|---|
| | | | | | Peak | Range | Uncertainty | Peak | Range | Uncertainty | Distance | Range | Uncertainty |
| g/cm$^3$ | nm | mm$^{-1}$ | mm | cm$^{-1}$ | cm$^{-1}$ | cm$^{-1}$ | cm$^{-1}$ | cm$^{-1}$ | cm$^{-1}$ | cm$^{-1}$ | cm$^{-1}$ | cm$^{-1}$ | cm$^{-1}$ |
| 0.1477 | 532.04 | 1800 | 800 | 0.272 | 1285.150 | ±0.017 | ±0.062 | 1388.265 | ±0.011 | ±0.062 | 103.115 | ±0.012 | ±0.124 |
| | 632.816 | 600 | 800 | 0.671 | 1284.493 | ±0.045 | ±0.131 | 1387.615 | ±0.050 | ±0.131 | 103.123 | ±0.025 | ±0.262 |
| | 532.02 | 1800 | 300 | 1.415 | 1284.493 | ±0.17 | ±0.1316 | 1387.608 | ±0.17 | ±0.1316 | 103.117 | ±0.10 | ±0.263 |
| | 632.817 | 600 | 800 | 1.076 | 1284.987 | ±0.028 | ±0.126 | 1388.119 | ±0.027 | ±0.126 | 103.132 | ±0.030 | ±0.252 |
| 0.8880 | 532.02 | 1800 | 300 | 1.416 | 1282.726 | ±0.085 | ±0.1316 | 1387.430 | ±0.058 | ±0.1316 | 104.704 | ±0.070 | ±0.263 |
| | 632.816 | 600 | 800 | 0.671 | 1281.581 | ±0.073 | ±0.131 | 1386.290 | ±0.068 | ±0.1310 | 104.709 | ±0.010 | ±0.262 |

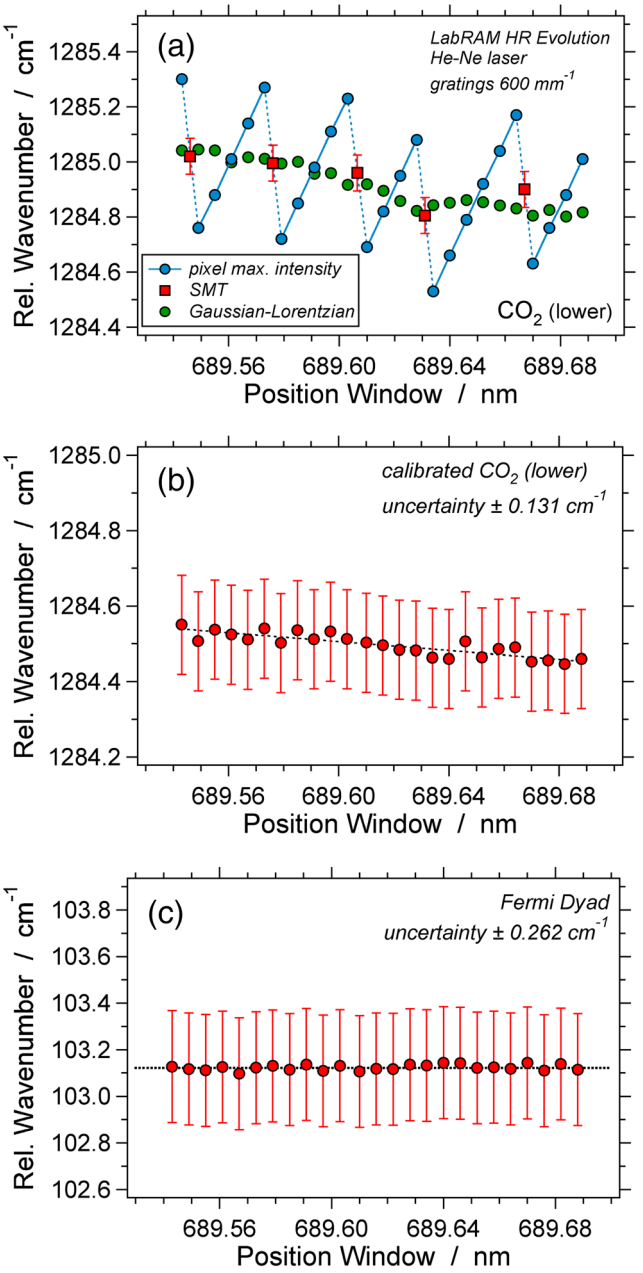


FIGURE 18 (a) Relative wavenumber of peak position of the lower band of $CO_2$ of the 0.1477 g·cm$^{-3}$ fluid inclusion as a function of spectral window position, estimated with *SMT* and symmetric Gaussian–Lorentzian curves using the LabRAM HR Evolution system with He–Ne laser; (b) calibrated relative wavenumbers of the lower band of $CO_2$, error bars illustrate the *SMT* uncertainty; (c) calibrated wavenumber distance of the Fermi dyad [Colour figure can be viewed at wileyonlinelibrary.com]

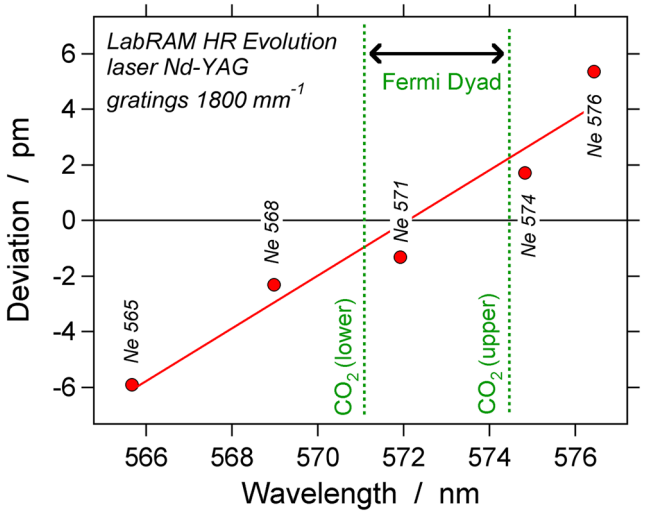


FIGURE 19 Deviation between theoretical and measured wavelength of neon lines as a function of absolute wavelength of these lines, which are used to calibrate the $CO_2$ spectrum (*Fermi dyad*) according to the proper bracketing technique (see paragraph 6.2) [Colour figure can be viewed at wileyonlinelibrary.com]

Fermi dyad of $CO_2$ in this example. First, the method of Lin et al.[18] and uncorrected values result in a Fermi dyad distance of 3.3800 nm (103.018 cm$^{-1}$). Then, the use of a line segment outside the wavenumber range of the $CO_2$ spectrum with the *576* and *574* neon line (cf. Wang et al.[40]) results in a significant correction of the Fermi dyad, that is, +7.7 pm (103.251 cm$^{-1}$), which is nearly the size of one pixel. Bracketing the spectrum with two neon lines, for example, *568* and *576* (cf. Lamadrid et al.[2]) results in a correction of +3.5 pm (103.124 cm$^{-1}$). The calibration of individual Raman bands can be obtained by a simple linear regression defined by 3, 4, and 5 neon lines (see paragraph 6.2), that completely enclose the $CO_2$ spectrum (both lower and upper $CO_2$ band). The resulting Fermi dyad is estimated at slightly higher values than the uncorrected value, that is, +1.0, +1.2, and +1.3 pm (103.048 to 103.057 cm$^{-1}$), respectively.

## 11.1 | $CO_2$ density: microthermometry versus Raman spectroscopy

Microthermometry is generally considered a better method to determine fluid density than Raman spectroscopic gas densimetry (e.g., Frezzotti et al.[63]). Therefore, gas densimeters should be mainly applied to inclusions that are not suitable for microthermometric analyses. A general definition of these type of inclusions is not applicable: inclusions as small as 2 μm may reveal microthermometric data; and homogenization modes into the vapor phase may be determined with an accuracy of ±0.1 degree (see examples in the paragraphs 10 "Case study 2: methane" and 11 "Case study 3: carbon dioxide"). Fall et al.[41] overestimated the uncertainties in both microthermometry and Raman spectroscopy

(Fermi dyad): ±0.05°C and ±0.035 $cm^{-1}$, respectively. These numbers are defined by statistical analyses, that is, average and standard deviations, and not related to uncertainty in individual measurements. Temperature measurements with Linkam heating-freezing stages provide a minimum uncertainty of ±0.1°C. Lamadrid et al.[2] estimated a $CO_2$ density error of ±0.0037 $g{\cdot}cm^{-3}$ corresponding to a highly overestimated uncertainty of the Fermi dyad (±0.01 $cm^{-1}$) based on the same statistical analyses. Sublett et al.[4] define average deviations of both individual $CO_2$ peaks and the Fermi dyad of ±0.02 $cm^{-1}$, corresponding to ±0.006 $g{\cdot}cm^{-3}$. These numbers suggest that Raman spectroscopic gas densimeters are similar in quality to microthermometric analyses (cf. ±0.0006 to ±0.0007 $g{\cdot}cm^{-3}$). The present study has illustrated that the correct uncertainties of $CO_2$ gas densimeters analyses with modern Raman equipment are in the range of ±0.26 $cm^{-1}$, which is a factor 150 less accurate than microthermometry.

Kobayashi et al.[64] directly compared $CO_2$ density values obtained by microthermometry and Raman spectroscopy, according to the gas densimeter equation of Yamamoto and Kagi,[48] and concluded that this Raman gas densimeter is "fairly consistent" with densities determined by microthermometry. In addition to numerous erroneous statements about the limits of microthermometry, the inconsistency of numerous published Raman gas densimeters was completely ignored. Table S2 reveals that the Yamamoto and Kagli[48] model results in highly inconsistent values of $CO_2$ density of the fluid inclusions presented in Figure 16. Remigi et al.[22] also present a perfect correlation between $CO_2$ density obtained from microthermometry and Fermi dyad distance. However, peak positions were not calibrated with simultaneously recorded reference lines, and the estimated correlation is instrument specific. The numerous uncertainties of Raman spectroscopic analyses that are illustrated in the present study and apparent inconsistencies of experimental data sets favor the use of microthermometry to model fluid inclusion $CO_2$ densities.

## 12 | CONCLUSIONS

Wavenumbers of Raman bands of gases can be used to determine fluid densities. However, modifications of Raman band peak positions are relatively small compared with the pixel resolution of CCD detectors. Not all the aspects of calibration have been adequately addressed in literature, and the variety of calibration methods resulted in numerous inconsistent empirical equations. Vibrational modes of gas molecules are fundamental properties, and the quantitative analyses of the energy involved in these processes must reveal consistent values independent of the machinery that is used to measure it. The main cause of apparent inconsistencies in published data sets is the lack of knowledge of uncertainty in individual measurements, which is often confused for reproducibility. Uncertainty is mainly defined by technical and mechanical properties of the Raman spectrometer, in addition to inappropriate digital signal processing. Reproduction of Raman band shapes with best-fit probability distribution functions provides peak positions, but not any information about the uncertainty of these positions. The use of different types of distribution functions may result in a large variety of shape properties.

The modified scanning multichannel technique is a new method to determine peak positions of Raman bands without mathematical manipulations to define peak shapes. In addition, this method determines a well-defined uncertainty of individual measurements. The method uses the minimum step size of relocating the gratings that moves the position of the spectral window by a fraction of the pixel size. The intensity modification of adjacent pixels can be used to define the best estimate of a peak position, with an uncertainty equal to the step size of the gratings rotation (in nm).

The Raman system is able to reproduce the wavelength of a He–Ne laser with a variability of 3 pm (632.816 ± 0.003 nm). This is also the minimum variability for Raman bands, whose uncertainty is subsequently further increased by the selected reference materials. The use of silicon and benzonitrile as reference Raman bands may increase wavenumber uncertainties up to 1 $cm^{-1}$. Atomic emission lines provide the best reference material, due to their relatively narrow shape. They must be recorded simultaneously with Raman bands and must be included within the same spectral window to be able to calibrate the Raman band peak positions. Higher resolutions of Raman spectrometers do not necessary improve the method, because the size of a spectral window will be largely reduced, and consequently specific reference lines cannot anymore be simultaneously detected.

The signal of a solid state laser, for example, a frequency doubled ND–YAG laser, must be calibrated with the proposed method before any measurement session because its wavelength is highly sensitive to variable laboratory conditions.

A major drawback of the method is the mechanical irregularities of the Sinus Arm Drive system, which rotates the gratings. Peak positions are affected by the relative position within a spectral window, and the positions can drift after movement of the drive over larger

angles. Improvements in the design of the spectrometer may minimize this effect and rank the proposed method to the most accurate estimation of peak positions at a subpixel scale.

The most practical analytical procedure with modern Raman spectrometers can be summarized by as follows: (1) define a general uncertainty of Raman band peak position with the modified scanning multichannel technique; (2) use a best-fit probability distribution function to determine a peak position; (3) define its uncertainty as twice the value obtain in the first step.

A $CO_2$ density of $0.1477 \pm 0.0006$ g·cm$^{-3}$ and $0.8880 \pm 0.0007$ g·cm$^{-3}$ determined with microthermometry correspond to a Fermi dyad of $103.12 \pm 0.27$ cm$^{-1}$ and $104.71 \pm 0.26$ cm$^{-1}$. A $CH_4$ density of $0.3461 \pm 0.0002$ g·cm$^{-3}$ and $0.4011 \pm 0.0001$ g·cm$^{-3}$ correspond to a Raman band peak position of $2910.66 \pm 0.12$ cm$^{-1}$ and $2910.57 \pm 0.12$ cm$^{-1}$. The error in these numbers must be regarded as the best estimated uncertainties of Raman band peak positions, which are probably slightly adjusted to higher values due to irregularities of the Sinus Arm Drive of Raman systems. The estimated peak positions are consistent between different Raman system. The numerous inconsistent gas densimeters presented in literature could be unified in a single equation by considering the uncertainties as defined in the present study.

## ACKNOWLEDGEMENTS

Two anonymous reviewers are thanked for their critical reviews of the manuscript.

## DATA AVAILABILITY STATEMENT

Data available in article

## ORCID

*Ronald J. Bakker* https://orcid.org/0000-0001-9427-2784

## REFERENCES

[1] J. Zhang, S. Qiao, W. Lu, Q. Hu, S. Chen, Y. Liu, *J. Geochem. Explor.* **2016**, *171*, 20.
[2] H. M. Lamadrid, I. R. Moore, D. Moncada, J. D. Rimstidt, R. C. Burruss, R. J. Bodnar, *Chem. Geol.* **2017**, *450*, 210.
[3] Y. Hagiwara, K. Takahata, J. Torimoto, J. Yamamoto, *J. Raman Spectrosc.* **2018**, *49*, 1776.
[4] D. M. Sublett Jr., E. Sendula, H. Lamadrid, M. Steele-MacInnes, G. Spiekermann, R. C. Burruss, R. J. Bodnar, *J. Raman Spectrosc.* **2020**, *51*, 555.
[5] F. Rull, in *Raman Spectroscopy Applied to Earth Sciences and Cultural Heritage*, (Eds: J. Dubessy, M. C. Caumon, F. Rull), European Mineralogical Union and the Mineralogical Society of Great Britain and Ireland, London **2012** 1.
[6] J. F. Bertrán, *Spectrochim. Acta* **1983**, *39a*, 119.
[7] Y. Garrabos, V. Chandrasekharan, M. A. Echargui, F. Marsault-Herail, *Phys. Lett.* **1989**, *160*, 250.
[8] R. Span, W. Wagner, *J. Phys. Chem. Ref. Data* **1996**, *25*, 1509.
[9] U. Setzmann, W. Wagner, *J. Phys. Chem. Ref. Data* **1991**, *20*, 1061.
[10] H. O. Hamaguchi, *Appl. Spectrosc. Rev.* **1988**, *24*, 137.
[11] D. A. Carter, J. E. Pemberton, *Appl. Spectrosc.* **1995**, *49*, 1550.
[12] R. W. Berg, T. Nørbygaard, *Appl. Spectrosc. Rev.* **2006**, *41*, 165.
[13] P. Knoll, R. Singer, W. Kiefer, *Appl. Spectrosc.* **1990**, *44*, 776.
[14] V. Deckert, W. Kiefer, *Appl. Spectrosc.* **1992**, *46*, 322.
[15] D. A. Sadler, D. Littlejohn, R. Riley, C. V. Perkins, *Appl. Spectrosc.* **1996**, *50*, 504.
[16] E. S. Izraeli, J. W. Harris, O. Navon, *Earth Plan. Sci. Lett.* **1999**, *173*, 351.
[17] S. Fukura, T. Mizukami, S. Odake, H. Kagi, *Appl. Spectrosc.* **2006**, *60*, 946.
[18] F. Lin, R. J. Bodnar, S. P. Becker, *Geochim. Cosmochim. Acta* **2007**, *71*, 3746.
[19] E. B. Saloman, C. J. Sansonetti, *J. Phys. Chem. Ref. Data* **2004**, *33*, 1113.
[20] W. Lu, I. M. Chou, R. C. Burruss, Y. Song, *Geochim. Cosmochim. Acta* **2007**, *71*, 3969.
[21] V.-H. Le, M.-C. Caumon, A. Tarantola, *Comp. Geosc.* **2021**, *156*, 104896.
[22] S. Remigi, T. Mancini, S. Ferrando, M. L. Frezzotti, *Appl. Spectrosc.* **2021**, *75*, 867.
[23] T. J. Shepherd, A. H. Rankin, D. H. M. Alderton, *A Practical Guide to Fluid Inclusion Studies*, Blackie & Son Ltd, Glasgow **1985**.
[24] P. De Bièvre, *Accred. Qual. Assur.* **2008**, *13*, 61.
[25] M. Drosg, *Dealing with uncertainties, a guide to error analysis*, Springer, Heidelberg **2009**.
[26] G. Turrell, J. Corset, *Raman Spectroscopy, Developments and Applications*, Elsevier Academic Press, Amsterdam **1996**.
[27] D. Tuschel, *Spectroscopy* **2020**, *35*, 9.
[28] K. M. Rosso, R. J. Bodnar, *Geochim. Cosmochim. Acta* **1995**, *59*, 3961.
[29] D. Hutsebaut, P. Vandenabeele, L. Moens, *Analyst* **2005**, *130*, 1204.
[30] D. A. Carter, W. R. Thompson, C. E. Taylor, J. E. Pemberton, *Appl. Spectrosc.* **1995**, *49*, 1561.
[31] T. J. Vickers, C. K. Mann, *Appl. Spectrosc.* **1999**, *53*, 1617.
[32] X. Yuan, R. A. Mayanovic, *Appl. Spectrosc.* **2017**, *71*, 232.
[33] J. Dubessy, M.-C. Caumon, F. Rull, S. Sharma, in *Raman Spectroscopy Applied to Earth Sciences and Cultural Heritage*, (Eds: J. Dubessy, M.-C. Caumon, F. Rull), European Mineralogical Union and the Mineralogical Society of Great Britain and Ireland, London **2012** 83.
[34] Y. Hagiwara, J. Torimoto, J. Yamamoto, *J. Raman Spectrosc.* **2020**, *51*, 1003.
[35] Y. Morizet, M. Paris, F. Gaillard, B. Scaillet, *Chem. Geol.* **2009**, *264*, 58.
[36] M.-C. Caumon, P. Robert, E. Laverret, A. Tarantola, A. Randi, J. Pironon, J. Dubessy, J. P. Girard, *Chem. Geol.* **2014**, *378–379*, 52.
[37] V.-H. Le, M.-C. Caumon, A. Tarantola, A. Randi, P. Robert, J. Mullis, *Anal. Chem.* **2019**, *91*, 14359.
[38] J. C. Seitz, J. D. Pasteris, I. M. Chou, *Am. J. Sci.* **1993**, *293*, 297.

[39] R. L. McCreery, *Raman Spectroscopy for Chemical Analysis*, John Wiley & Sons **2000**.
[40] W. Wang, M.-C. Caumon, A. Tarantola, J. Pironon, W. Lu, Y. Huang, *Chem. Geol.* **2019**, *528*, 119281.
[41] A. Fall, B. Tattitch, R. J. Bodnar, *Geochim. Cosmochim. Acta* **2011**, *75*, 951.
[42] S. B. Kim, R. M. Hammaker, W. G. Fateley, *Appl. Spectrosc.* **1986**, *40*, 412.
[43] X. Wang, I. M. Chou, W. Hu, R. C. Burruss, Q. Sun, Y. Song, *Geochim. Cosmochim. Acta* **2011**, *75*, 4080.
[44] L. Shang, I. M. Chou, R. C. Burruss, R. Hu, X. Bi, *J. Raman Spectrosc.* **2014**, *45*, 696.
[45] A. Takamizama, S. Yanagimachi, T. Ikegami, *Appl. Phys. Express* **2016**, *9*, 032704.
[46] D. Liu, H. Byrne, L. O'Neill, B. M. Hennelly, *Proc. SPIE* **2018**, 10680, 27.
[47] Y. Kawakami, J. Yamamoto, H. Kagi, *Appl. Spectrosc.* **2003**, *57*, 1333.
[48] J. Yamamoto, H. Kagi, *Chem. Lett.* **2006**, *35*, 610.
[49] N. Itho, K. Shirono, *J. Raman Spectrosc.* **2020**, *51*, 2496.
[50] Y. Song, I. M. Chou, W. Hu, R. Burruss, W. Lu, *Acta Geol. Sin.* **2009**, *83*, 932.
[51] J. H. Parker Jr., D. W. Feldman, M. Ashkin, *Phys. Rev.* **1967**, *155*, 712.
[52] T. R. Hart, R. L. Aggarwal, B. Lax, *Phys. Rev. B* **1970**, *1*, 638.
[53] M. Delhaya, J. Barbillat, J. Aubard, M. Bridoux, E. Da Silva, in *Raman Microscopy, Developments and Applications*, (Eds. G. Turrell, J. Corset), Elsevier Academic Press, Amsterdam, **1996**, pp. 51–174.
[54] G. R. Hopkinson, T. M. Goodman, S. R. Prince, *A Guide to the Use and Calibration of Detector Array Equipment*, SPIE, Bellingham (USA) **2004**.
[55] R. J. Bakker, E. Pushkarev, A. P. Biryuzova, J. Petrol. **2020**; *61*, egaa066.
[56] R. J. Bakker, *Chem. Geol.* **2003**, *194*, 3.
[57] R. J. Bakker, *Ber. Geol. Bund.* **2011**, *87*, 32.
[58] R. J. Bakker, J. B. H. Jansen, *Geochim. Cosmochim. Acta* **1991**, *55*, 2215.
[59] R. J. Bakker, *Minerals* **2017**, *7*, 117.
[60] E. Fermi, *Zeitschrift für Phys.* **1931**, *71*, 250.
[61] A. Langseth, J. R. Nielsen, *Z. Phys. Chem. B* **1932**, *19*, 427.
[62] E. A. J. Burke, *Lithos* **2001**, *55*, 139.
[63] M. L. Frezzotti, F. Tecce, A. Casagli, *J. Geochem. Expl.* **2012**, *112*, 1.
[64] T. Kobayashi, J. Yamamoto, T. Hirajima, H. Ishibashi, N. Hirano, Y. Lai, V. S. Prikhod'ko, S. Arai, *J. Raman Spectrosc.* **2012**, *43*, 1126.

## SUPPORTING INFORMATION

Additional supporting information may be found in the online version of the article at the publisher's website.

**How to cite this article:** R. J. Bakker, *J Raman Spectrosc* **2021**, 1. https://doi.org/10.1002/jrs.6245